Available online at www.sciencedirect.com
ScienceDirect
Coastal Engineering 55 (2008) 1–20
Coastal Engineering
An International Journal for Coastal, Harbour and Offshore Engineers
www.elsevier.com/locate/coastaleng

Wave boundary layer over a stone-covered bed

Martin Dixen, Figen Hatipoglu [1], B. Mutlu Sumer *, Jørgen Fredsøe

Technical University of Denmark, MEK, Coastal, Maritime and Structural, Engineering Section (formerly ISVA), DK-2800 Kgs. Lyngby, Denmark

Received 1 May 2006; received in revised form 10 January 2007; accepted 18 June 2007
Available online 14 August 2007

Abstract

This paper summarizes the results of an experimental investigation on wave boundary layers over a bed with large roughness, simulating stone/rock/armour block cover on the sea bottom. The roughness elements used in the experiments were stones the size of 1.4cm and 3.85cm in one group of experiments and regular ping-pong balls the size 3.6cm in the other. The orbital-motion-amplitude-to-roughness ratio at the bed was rather small, in the range $a/k_s = 0.6$–3. The mean and turbulence properties of the boundary-layer flow were measured. Various configurations of the roughness elements were used in the ping-pong ball experiments to study the influence of packing pattern, packing density, number of layers and surface roughness of the roughness elements. The results show that the friction factor seems to be not extremely sensitive to these factors. The results also show that the friction factor for small values of the parameter a/k_s does not seem to tend to a constant value as $a/k_s \to 0$ (contrary to the suggestion made by some previous investigators). The present friction-factor data indicates that the friction factor constantly increases with decreasing a/k_s. An empirical expression is given for the friction factor for small values of a/k_s. The results further show that the phase lead of the bed friction velocity over the surface elevation does not seem to change radically with a/k_s, and found to be in the range 12°–23°. Furthermore the results show that the boundary-layer turbulence also is not extremely sensitive to the packing pattern, the packing density, the number of layers and the surface roughness of the roughness elements. There exists a steady streaming near the bed in the direction of wave propagation, in agreement with the existing work. The present data indicate that the steady streaming is markedly smaller in the case where the ping-pong balls are aligned at 45° to the wave direction than in the case with 90° alignment. Likewise, it is found that the steady streaming is relatively smaller in the case of the one-layer ping-pong-ball roughness than in the case of the two-layer situation.

1. Introduction

The behaviour of wave boundary layers at small values of the roughness parameter a/k_s is important, for instance, in connection with the investigations of the stability of rip-rap scour protection in the marine environment where large size of stones/rock/armour blocks inevitably leads to small values of a/k_s ($a/k_s = O(1)$, or smaller) in which a is the amplitude of the orbital motion at the bed and k_s Nikuradse's equivalent sand roughness, which may be taken as 2–2.5D, as will be detailed in the paper, D being the size of the roughness elements (stones/rock/armour blocks).

Of particular interest is the flow resistance, characterized by the wave friction factor, f_w. In his famous drum experiments, Bagnold (1946) obtained experimental evidence for a special behaviour of the wave friction factor, at very small values of a/k_s, namely f_w approaches a constant value at very small values of a/k_s as $a/k_s \to 0$. This observation has puzzled many scientists since no mathematical or numerical modelling has been able to predict this behaviour, but rather they have predicted an increase in f_w even at very small a/k_s ratios with decreasing a/k_s, see e.g. Justesen (1988a,b). Sleath (1984), from theoretical considerations (which will be detailed later), concluded that f_w should vary $f_w \propto (a/k_s)^{-1}$ as $a/k_s \to 0$.

The purpose of the present paper is to shed more light on the hydrodynamic behaviour of the wave boundary layer by presenting detailed flow data in the small a/k_s-environment. The data can be viewed as complementary to those presented earlier by Kamphuis (1975), Sleath (1984) and Simons et al. (2000). The paper essentially presents the results of two experimental campaigns. In an attempt to get data for the wave friction factor for beds covered with stones/armour blocks, a series of experiments were carried out with stones the size 3.85cm and 1.4cm in a wave flume. Early results of these experiments were reported

* Corresponding author. Fax: +45 45 93 53 28.
E-mail address: bms@mek.dtu.dk (B.M. Sumer).
[1] On leave from Istanbul Technical University, Faculty of Civil Engineering, Maslak 34469 Istanbul, Turkey.

0378-3839/$ - see front matter © 2007 Elsevier B.V. All rights reserved.
doi:10.1016/j.coastaleng.2007.06.005

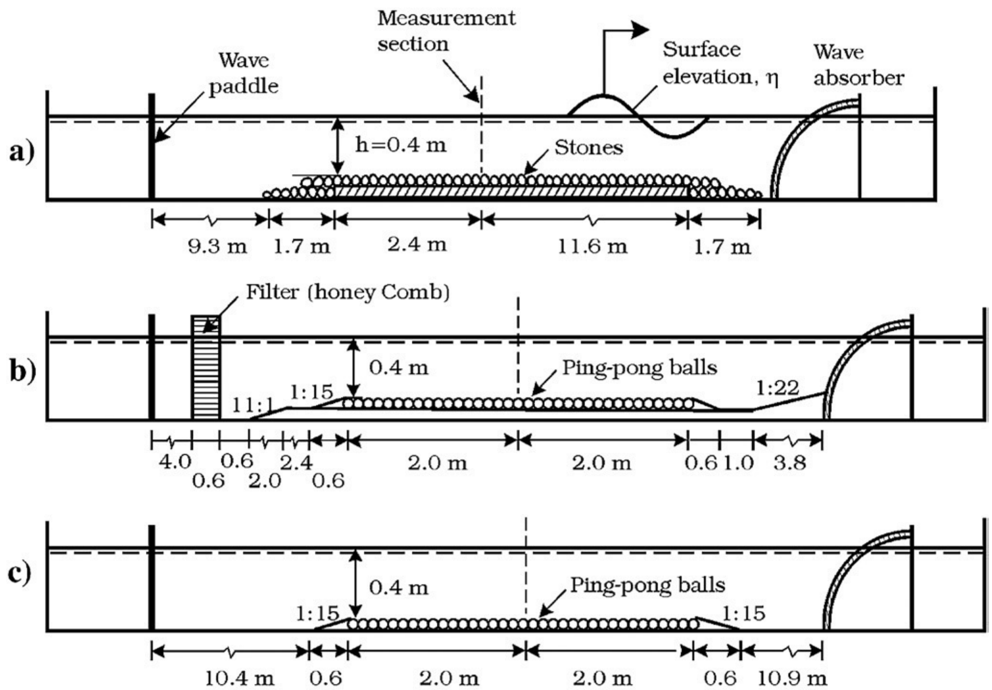

Fig. 1. Experimental set-up. (a) Flume A (Tests S1–S3). (b) Flume B (Tests P1 and P2). (c) Flume A (Tests P3–P5).

in Hatipoglu et al. (2004). The findings of this investigation brought up new questions such as (1) What is the effect of the orientation of the roughness elements with respect to the direction of flow/wave propagation? (2) What is the effect of the number of layers of roughness elements? (3) What is the effect of the surface roughness of the roughness elements? (4) How does the friction velocity (the key quantity for the calculation of the friction factor) found from the classic log-fit method compare with that obtained from the so-called momentum-integral method? To address these questions, a new series of experiments were conducted, this time, with a well-defined roughness-element geometry, namely spheres (ping-pong balls the size D=3.6cm). Although not as comprehensive as the second series of the experiments, it was felt that the results of the first

Table 1
Roughness material and characteristic properties of the bed roughness plus the wave flumes used

Test	Roughness material	Size of roughness elements, D (cm)	Packing pattern, orientation of roughness elements and number of layers	Surface of individual roughness elements	Images of the roughness elements	Wave flume
(1)	(2)	(3)	(4)	(5)	(6)	(7)
S1	Stones	3.85	• Dense packing • Random orientation • 1-layer deep	Hydraulically smooth	Fig. 2a	Flume A (Fig. 1a): • No Active Wave Absorption System (AWACS) • False bottom
S2	”	”	”	”	”	”
S3	”	1.4	”	”	Fig. 2b	”
P1	Ping-pong balls	3.6	• Cubic packing • 90° orientation • 1-layer deep	Hydraulically smooth	Fig. 2c	Flume B (Fig. 1 b) • No AWACS • False bottom
P2	”	”	• Cubic packing • 90° orientation • 2-layer deep	”	Fig. 2d	”
P3	”	”	• Cubic packing • 45° orientation • 1-layer deep	”	Fig. 2e	Flume A (Fig. 1c): • With AWACS • No false bottom
P4	”	”	• Cubic packing • 90° orientation • 1-layer deep	”	Fig. 2c	”
P5	”	”	• Cubic packing • 90° orientation • 1-layer deep	Roughened with sand the size 1.5 mm	Fig. 2f	”

series of the experiments with stones also should be included in the present report since they complement the results obtained from the ping-pong-ball tests.

2. Experimental facility

2.1. Wave flume

The tests were carried out in two wave flumes: Flume A (28m × 0.80m (depth) × 0.60m (width)) and Flume B (25m × 0.80m (depth) × 0.60m (width)), Fig. 1a–c and Table 1.

Flume A was used for both stone- and ping-pong-ball experiments (Fig. 1a and c, and Table 1, Tests S1–S3 and P3–P5) while Flume B was used for ping-pong-ball experiments (Fig. 1b, and Table 1, Tests P1 and P2), as will be detailed later.

Two notes with regard to the experimental flumes are:

1. Flume A was, prior to the second experimental campaign with ping-pong balls, equipped with the DHI AWACS system, enabling simultaneous generation of desired waves and absorption of the associated reflected waves (Schaffer et al., 1994). With this system switched on, three tests were carried out in the second campaign of the experiments (Tests P3–P5, Table 1).
2. The 3.8m long section with a slope of 1:22 at the onshore end of Flume B (Fig. 1b) was present before the Tests P1 and P2, and no attempt was made to change it to a horizontal bed. The consequence of the latter will be discussed later in conjunction with the steady streaming in the flume.

Regular waves were produced by a piston type wave generator in both flumes.

2.2. Roughness material

Two kinds of bed roughness were used: (1) stones and (2) ping-pong balls (Table 1). The motivation behind the selection of these roughness types is given under Introduction section.

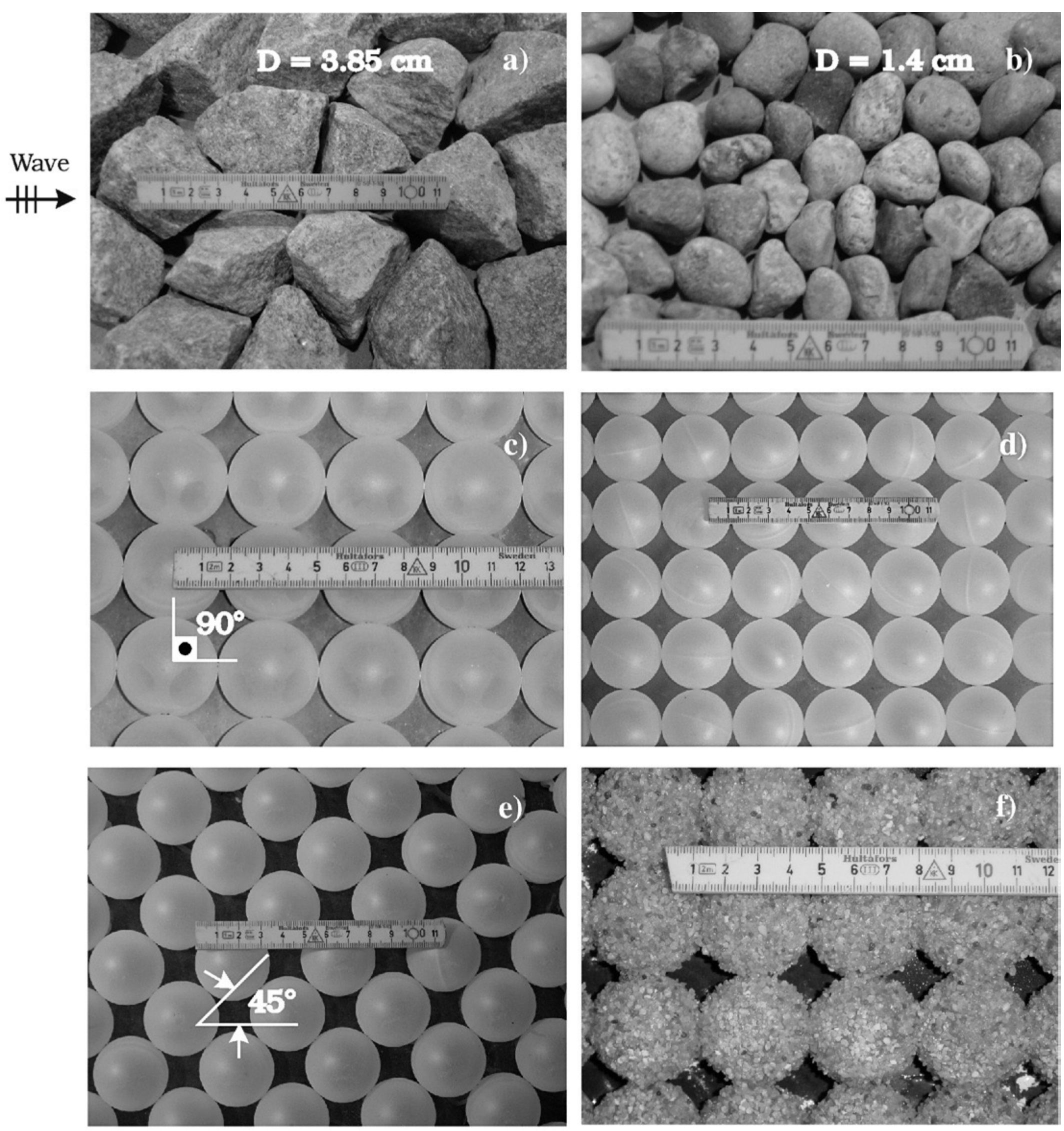

Fig. 2. Roughness elements (a)–(b): stones. (c)–(f): ping-pong balls.

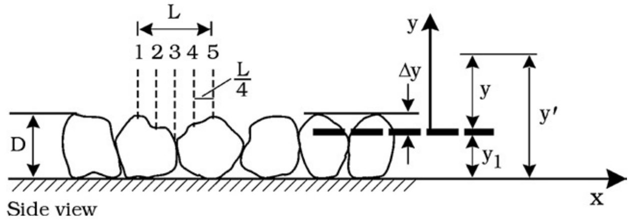

Fig. 3. Measurement verticals (1, 2, 3, 4 and 5) and definition sketch in the case of the stone experiments.

The stones were placed in a single layer on the bottom of the flume over a length of 14m. They were carefully levelled off. The stone section ended with two ramps at the two ends with a slope of about 1:15. Two kinds of stones the size of D=3.85 and 1.4cm were used (Fig. 2a and b respectively). Here D is the mean stone size. The latter was found in the following way. Stones were dumped on the bottom of the flume and subsequently arranged in a dense packing (Figs. 2a and b). Then the mean height was measured over a sample of 30 stones. The mean height obtained this way, D=3.85 and 1.4cm (Fig. 3), was designated as the mean stone size, and is equivalent to the so-called mean roughness height (not to be confused by k_s, Nikuradse's equivalent sand roughness). The standard deviations corresponding to the samples were σ_D=0.67cm for the 3.85cm stones, and σ_D=0.26cm for the 1.4cm stones. The orientation of stones was random. The 3.85cm stones were angular while the 1.4cm stones were round. Three tests were carried out with stones, Tests S1–S3 (Table 1). Tests S1 and S2 were conducted with the same bed but with two different wave heights (Table 2).

Regarding the ping-pong balls, the arrangement of the ping-pong balls in the tests corresponds to the so-called cubic packing, illustrated in Fig. 2c–f (Lambe and Whitman, 1969, p. 31, can be consulted for various packing patterns for spheres). The cubic packing corresponds to the loosest packing pattern. One of the issues studied in the present work is the influence of the orientation of roughness elements with respect to the direction of wave propagation/flow. This may be studied with other packing patterns as well, such as the so-called hexagonal array. However, the latter arrangement corresponds to a denser packing. To avoid one more parameter involved in the investigation (namely the packing density), all the ping-pong ball tests were carried out with one, single packing density, corresponding to the cubic packing.

The ping-pong balls (the size D=3.6cm) were glued on a PVC plate (2cm thick), and then the PVC plate was rigidly fixed to the bottom of the flume. Five tests were conducted with the ping-pong balls, Tests P1–P5 (Table 1). The ping-pong balls were one-layer deep in Tests P1 and P3–P5 while they were two-layer deep in Test P2. The latter test was carried out to study whether or not the bed roughness affects the end results when it is more than one layer (the balls were glued on the bottom-layer balls to get the two-layer arrangement, Fig. 2d). In a single test, the orientation of the balls was 45° (Test P3, Fig. 2e), different from the rest of the ping-ball tests, 90°. This enabled us to study the influence of the orientation of the roughness elements on the end results.

2.3. Velocity measurements

2.3.1. Stone experiments

In these experiments (Tests S1–S3), the velocity measurements were made by a one component Laser Doppler Anemometer (LDA), a Dantec LDA-04 System with a 15mW He–Ne laser, which was used in forward-scatter mode. The system was equipped with a Dantec 55N10 frequency shifter and a Dantec 55N20 frequency tracker. The surface elevation, η, was measured with an ordinary resistance type wave gauge. η served as a reference signal in the data analysis. Sampling frequency was 20Hz, and 40 waves were recorded for each run.

2.3.2. Ping-pong-ball experiments

In the ping-pong-ball experiments (Tests P1–P5), the velocity measurements were made with a DANTEC two-component LDA equipped with a DANTEC 55N12 frequency shifter and a DANTEC 55N21 frequency tracker. The laser was a 300mW argon-ion laser and it was used in back-scatter mode for Tests P1–P2 and forward-scatter mode for Tests P3–P5. In the former tests, the glass side wall opposite to the side where the laser was placed was heavily scratched, and therefore the back-scatter mode was adopted. In the latter tests, however, the forward-scatter mode was preferred to get even a better quality signal. Similar to the stone tests, the surface elevation, η, was measured with an ordinary resistance type wave gauge, and η served as a reference signal in the data analysis. Sampling frequency in these tests was 220Hz, and 80 waves were recorded for each run. (1) The relatively high-frequency sampling rate and (2)

Table 2
Test conditions for the *stone* experiments

Test	H (cm)	T (s)	Crest/trough half period	U_m (cm/s)	a (cm)	k_s (cm)	a/k_s	Re	U_{fm} (cm/s)	f_w	φ (degrees)	Mean a/k_s	Mean Re	Mean U_{fm} (cm/s)
(1)	(2)	(3)	(4)	(5)	(6)	(7)	(8)	(9)	(10)	(11)	(12)	(13)	(14)	(15)
S1	14.5	1.6	Crest	30.4	7.4	9	0.83	2.1×10^4	12.5	0.34	23	0.70	1.6×10^4	11.3
			Trough	22.6	5.2	9	0.58	1.1×10^4	10.1	0.40	20			
S2	17	1.6	Crest	34.0	8.1	9	0.90	2.6×10^4	11.7	0.24	19	0.73	1.9×10^4	10.1
			Trough	22.4	5.0	9	0.56	1.1×10^4	8.5	0.29	23			
S3	16.0	1.6	Crest	30.5	7.4	2.5	3.0	2.1×10^4	7.15	0.11	20	2.2	1.5×10^4	6.3
			Trough	23.7	4.0	3	1.3	9.0×10^3	5.5	0.11	21			

The water depth is h=0.4 m. U_{fm} values given in column 10 are determined from the log-fit method. Water temperature is 18 °C, and the water kinematic viscosity is $\nu=1.0646\times10^{-2}$ cm^2/s.

Table 3
Test conditions for the *ping-pong-ball* experiments

Test	H (cm)	T (s)	Crest/trough half period	U_m (cm/s)	a (cm)	k_s (cm)	a/k_s	Re	U_{fm} (cm/s)	f_w	φ (degrees)	Mean a/k_s	Mean Re	Mean U_{fm} (cm/s)
(1)	(2)	(3)	(4)	(5)	(6)	(7)	(8)	(9)	(10)	(11)	(12)	(13)	(14)	(15)
P1	14.2	1.6	Crest	27.7	6.0	9.1	0.66	1.6×10^4	13.0	0.44	20	0.75	1.7×10^4	11.8
			Trough	25.0	7.4	8.9	0.83	1.7×10^4	10.6	0.36				
P2	14.2	1.6	Crest	27.9	6.1	9.0	0.68	1.6×10^4	13.6	0.48	19	0.74	1.7×10^4	11.9
			Trough	24.9	7.4	9.1	0.81	1.7×10^4	10.2	0.34				
P3	14.2	1.6	Crest	30.9	6.8	9.1	0.74	2.0×10^4	14.0	0.41	12	0.72	1.7×10^4	11.9
			Trough	23.1	6.3	9.0	0.71	1.4×10^4	9.8	0.36				
P4	14.2	1.6	Crest	32.5	7.2	9.0	0.79	2.2×10^4	13.8	0.36	16	0.72	1.7×10^4	11.9
			Trough	22.0	5.8	9.1	0.64	1.2×10^4	10.0	0.41				
P5	14.2	1.6	Crest	33.3	7.3	9.1	0.81	2.3×10^4	13.4	0.33	17	0.75	1.8×10^4	11.9
			Trough	22.7	6.3	9.0	0.69	1.3×10^4	10.4	0.41				

The water depth is h=0.4 m. U_{fm} values given in column 10 are determined from the log-fit method. Water temperature varied in the range 17.5–18.5 °C, and the water kinematic viscosity is taken as $\nu=1.0646\times10^{-2}$ cm²/s in the calculation of the Reynolds numbers in the table.

twice as many waves as in the previous experiment are adopted in these tests to ensure a flawless implementation of the momentum-integral method, one of the objectives of the second experimental campaign as mentioned in Section 1.

3. Test conditions

Test conditions in the stone experiments are given in Table 2. In the table, H is the wave height, T is the wave period, U_m is the maximum value of the orbital velocity measured at the distance y=4cm from the bed (representing the "potential-flow" orbital velocity at the bed), and a is the amplitude of the orbital motion of water particles at the same location, obtained from the integration in phase of the horizontal velocity from the zero-upcrossing point to the zero-downcrossing point for the crest half period and from the zero-downcrossing point to the zero-upcrossing point for the trough half period, namely, $a=\left(\int_{\text{zero-up}}^{\text{zero-down}} u\,dt\right)/2$ for the crest half period and similar for the trough half period. In the table, Re is the Reynolds number defined by

$$\mathrm{Re}=\frac{aU_m}{\nu} \tag{1}$$

in which ν is the kinematic viscosity. Furthermore, U_{fm} is the maximum value of the friction velocity, f_w the wave friction coefficient (Eq. (11)) and ϕ the phase lead of the friction velocity over the surface elevation.

Test conditions for the ping-pong-ball experiments are given in Table 3. The way in which k_s, U_{fm}, f_w and φ are calculated will be described later. Because of the relatively large wave heights, the oscillations were not symmetric between the crest and the trough. For that reason, the crest half period and the trough half period have been treated separately, Tables 2 and 3.

The water depth was h=0.4m in all the tests.

4. Ensemble- and space-averaged velocity profiles

In the ping-pong-ball experiments, the horizontal (x) and vertical (y) components of the velocity, $u(y,\omega t)$ and $v(y,\omega t)$, respectively, were measured at four verticals for the 90°-orientation arrangement (1, 2, 3 and 4, Fig. 4a), and at three verticals (1, 2 and 3, Fig. 4b, dropping Vertical 4 due to symmetry) for the 45°-orientation arrangement. Here, y=the distance from the bed, ω=the angular frequency and t=time. Ensemble-averaged velocity profiles, for example, for the u component

$$\overline{u}_i(y,\omega t)=\frac{1}{N}\sum_{j=1}^{N} u_i[y,\omega(t+(j-1)T)] \tag{2}$$

were calculated at each measurement vertical i in which i is the vertical number (i=1, 2, 3, 4, Fig. 4) and N the number of cycles sampled. Subsequently, the space-averaged velocity profiles, $<\overline{u}>$, were obtained from the four ensemble-averaged profiles according to

$$<\overline{u}>(y,\omega t)=\frac{1}{A}\int_A \overline{u}(y,\omega t)dA=\frac{\sum_{i=1}^{4}\overline{u}_i(y,\omega t)}{4} \tag{3}$$

in which A=the bed area over which the velocity is averaged. In the case of the 45°-orientation arrangement, $\overline{u}_4(y,\omega t)$ is taken identically equal to $\overline{u}_2(y,\omega t)$ in the above calculation (this is due to symmetry, Fig. 4b).

Regarding the stone experiments, these experiments were conducted in an attempt to provide data for the wave friction coefficient for beds covered with stones/armour blocks. As mentioned in the Introduction, we had no plans to conduct the ping-pong-ball experiments at the time. Therefore the way in

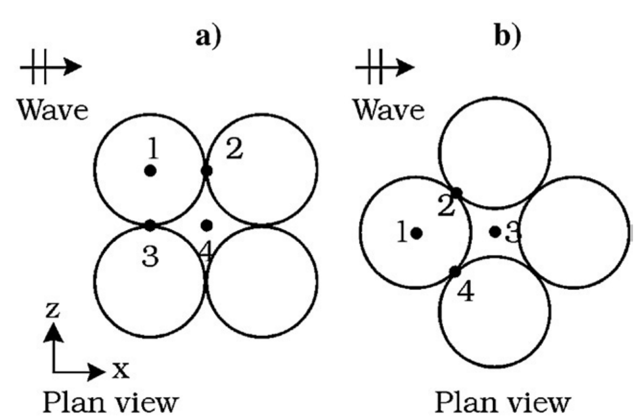

Fig. 4. Ping-pong balls. (a): 90°-arrangement. (b): 45°-arrangement.

which the space-averaged velocity profiles were calculated (or the way in which the velocity profile measurements were made) is somewhat different from that in the ping-pong-ball experiments. In these tests, the space-averaged velocity profiles, $<\overline{u}>$, were obtained from the five ensemble-averaged profiles according to

$$<\overline{u}>(y,\omega t) = \frac{\sum_{i=1}^{5} \overline{u}_i(y,\omega t)}{5} \quad (4)$$

in which the five velocity profiles $\overline{u}_i(y,\omega t)$ ($i=1,\ldots,5$) in the above equation were measured at five verticals (1,…, 5) indicated in Fig. 3, L being the crest-to-crest distance between the two neighbouring stones. This kind of space averaging may be not entirely correct as it does not include velocity variation in the transverse (z) direction. This inadequacy may be significant very near the bed, but is expected to disappear gradually as one moves away from the bed. Since it was felt that the results of these experiments also should be included in the present report as they complement the results obtained from the ping-pong-ball experiments, we have decided to include the space-averaged velocity profiles obtained through Eq. (4), and yet to interpret the results with extra caution.

5. Bed friction velocity

5.1. Bed friction velocity from log-fit method

Fig. 5 gives the ensemble- and space-averaged velocity profiles at different phase (ωt) values in Test P4 for the crest and

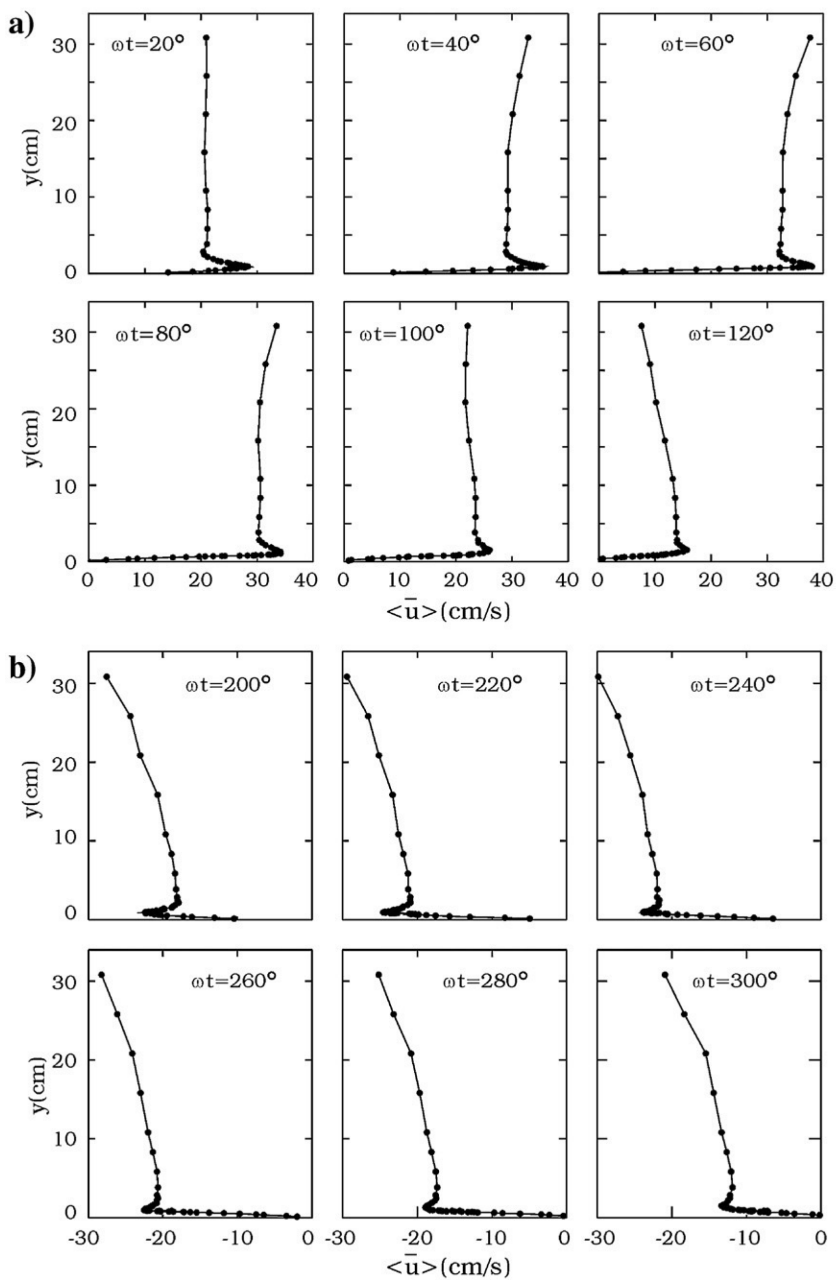

Fig. 5. Ensemble- and space-averaged velocity distributions. Test P4. Distance y is measured from the theoretical bed. (a) Crest half period. (b) Trough half period.

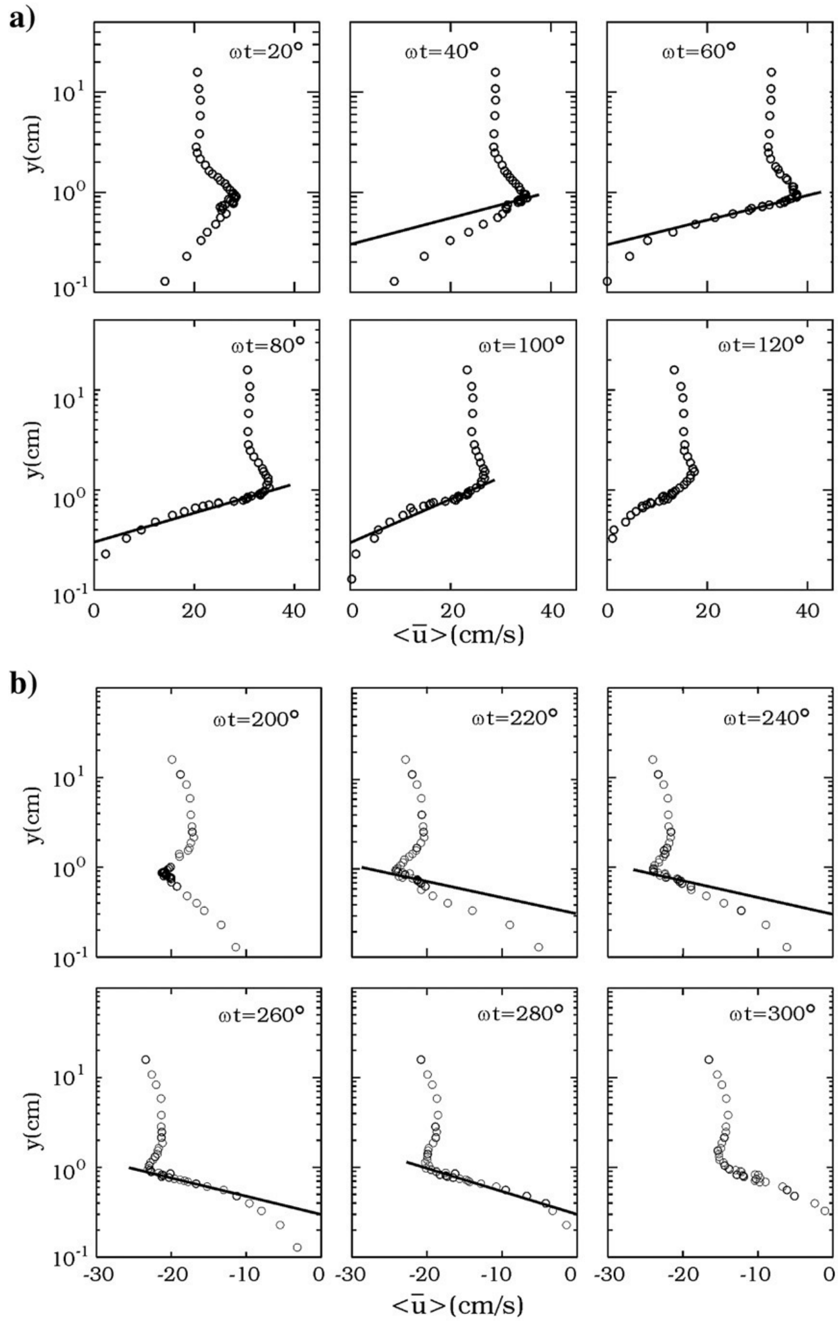

Fig. 6. Ensemble- and space-averaged velocity distributions. Test P4. Distance y is measured from the theoretical bed. Semi-logarithmic plot. (a) Crest half period. (b) Trough half period.

trough half periods, respectively, while Fig. 6 displays the same data in semi-log plots. Here, $\omega t=0$ corresponds to the zero upcrossing of the surface elevation signal. The velocity profiles for the other tests will not be given here for reasons of space. Now, the ensemble- and space-averaged velocity near the bed satisfies the logarithmic law provided that the boundary layer is thick enough to accommodate the logarithmic layer in it:

$$<\overline{u}>(y,\omega t)=\frac{U_{\mathrm{f}}}{\kappa}\ln\left(\frac{30(y'-y_1)}{k_{\mathrm{s}}}\right). \tag{5}$$

This occurs only after the boundary layer develops quite substantially in the phase space (for ωt values larger than about 40° for the present tests). Here $U_{\mathrm{f}}=U_{\mathrm{f}}(\omega t)$=the friction velocity, κ is the Kármán constant, $\kappa=0.4$, k_{s} is Nikuradse's equivalent sand roughness, y is the distance from the base bottom, and $y'-y_1=y$ is the distance from the theoretical bed (Fig. 7; see also Fig. 3 for a definition sketch for the stone case). The logarithmic law with y is then

$$<\overline{u}>(y,\omega t)=\frac{U_{\mathrm{f}}}{\kappa}\ln\left(\frac{30y}{k_{\mathrm{s}}}\right). \tag{6}$$

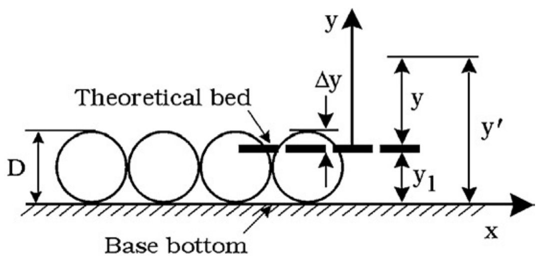

Fig. 7. Definition sketch.

Now, the friction velocity, U_f, is obtained from the measured velocity profiles at different phase (ωt) values by the following procedure:

1. Plot $<\overline{u}>$ $(y,\omega t)$ in a semi-logarithmic graph for various values of y_1.
2. Identify the straight-line portion of each curve.
3. For this, see the interval $0.2k_s \leq y \leq (0.2–0.3)\delta$. This is the interval where the logarithmic layer lies. The upper boundary, $(0.2–0.3)\delta$ ensures that the y levels lie in the constant stress layer, while the lower boundary, $0.2k_s$, ensures that the variation of $<\overline{u}>$ with respect to y is not influenced by the boundary roughness (Grass, 1971, Fig. 4), two conditions necessary for the velocity distribution to satisfy the logarithmic law (Monin and Yaglom, 1973, pp. 288–289; see also Fredsøe et al., 1999).
4. Identify the case where the thickness of the logarithmic layer (i.e., where the velocity is represented with a straight line) is largest, and adopt the value of y_1 of this case as the location of the theoretical bed.
5. The straight-line portion of the velocity profile corresponding to the latter case has a slope equal to U_f/κ, Eq. (5). From the latter information, find U_f.
6. The extension of the straight-line portion of the identified curve intercepts the y-axis at the value equal to $k_s/30$. From this information, find k_s.

Fig. 8 presents an example of the friction velocity obtained from the preceding procedure (Item 5) as a function of ωt (Test P1). The maximum values of the bed friction velocity, U_{fm}, determined from these diagrams for each half periods for Test P1, and those determined from similar diagrams for the other tests are all indicated in Tables 2 and 3, column 10. We shall return to U_{fm} later.

The k_s values determined from the y-intercepts of the velocity profiles in Fig. 6, or similar velocity profiles for the other tests (Item 6 in the above procedure) are indicated in Tables 2 and 3 (column 7), and the average values (and the standard deviations) for the stones and the ping-pong balls are as follows:

Roughness material	Average value of k_s	Standard deviation, σ_{ks}	k_s/D
Stones, D=3.85cm	9.0cm	–	2.3
Stones, D=1.4cm	2.75cm	–	2.0
Ping-pong balls, D=3.6cm	9.0cm	0.17cm	2.5

The k_s/D values above are apparently in good agreement with those reported in the literature for steady boundary-layer flows, which are generally in the range k_s/D=2–4 (Bayazit, 1983).

The calculations also show (Item 4 in the above procedure) that the location of the theoretical bed y_1 (or alternatively the so-called displacement thickness $\Delta y = D - y_1$) is $\Delta y = 0.25D$ for the stone data and $0.23D$ for the ping-pong-ball data. These agree quite well with the data reported in the literature for steady boundary-layer flows, namely $\Delta y = (0.15–0.35)D$ (Bayazit, 1976, 1983).

5.2. Bed friction velocity from momentum-integral method

The bed friction velocity can also be determined from the momentum-integral method.

The in-line force on an individual roughness element (the ping-pong ball or the stone) can be "translated" to the bed shear stress as

$$\tau_0(\omega t) = \rho \int_0^\delta \frac{\partial}{\partial t}[<\overline{u}_0> - <\overline{u}>]\ dy + \frac{1-n}{A_{xz}}\left\{\frac{1}{2}\rho C_D A_{yz}<\overline{u}_0>|<\overline{u}_0>| + \rho C_M V \frac{d}{dt}<\overline{u}_0>\right\} \quad (7)$$

in which $\tau_0 = \rho U_f^2$ is the bed shear stress, $<\overline{u}>$ is the ensemble-and-space-averaged velocity (Eqs. (3) and (4)) and $<\overline{u}_0>$ the potential-flow velocity just outside the boundary layer.

There are two contributions. Each contribution is now considered individually.

5.2.1. The contribution $\rho \int_0^\delta \frac{\partial}{\partial t}[<\overline{u}_0> - <\overline{u}>]dy$

This is the shear stress transferred from the flow onto the part of the bottom above the theoretical bed; it is obtained by integrating the momentum equation across the boundary-layer thickness (Fredsøe, 1984; a short account of the latter is also given in Fredsøe and Deigaard, 1992, p. 20). Here the lower

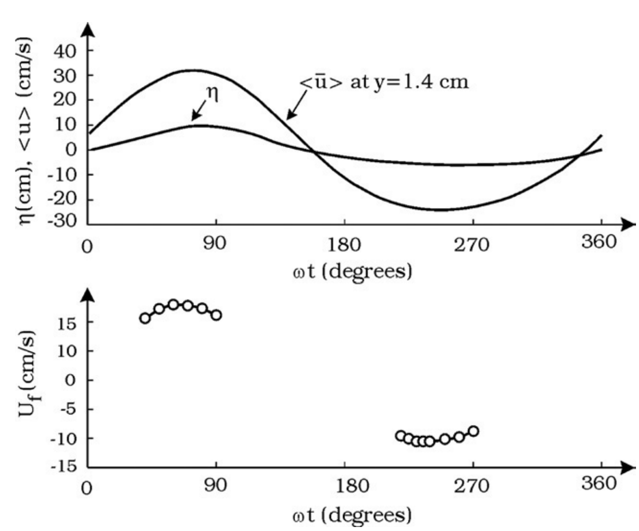

Fig. 8. Time variation of the ensemble- and space-averaged velocity at y=1.4 cm, the surface elevation and the friction velocity. Ping-pong ball experiments, Test P1.

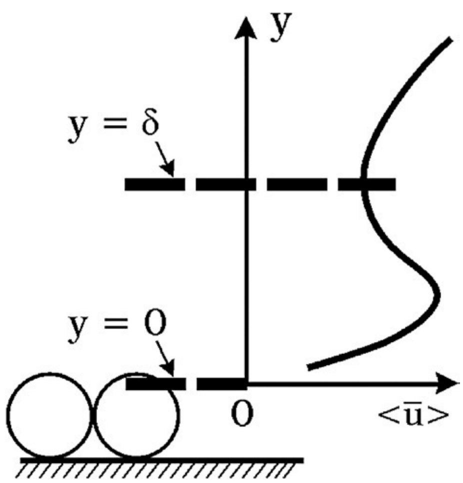

Fig. 9. Definition sketch for the momentum-integral method.

bound of the integral, $y=0$, corresponds to the theoretical bed (i.e., the elevation from which y in Eq. (6) is measured, and the upper bound, $y=\delta$, corresponds to the upper edge of the boundary layer (Fig. 9). This is the force on the "caps" of the individual roughness elements (i.e., Volume 1231, Fig. 10).

5.2.2. The contribution $\frac{1-n}{A_{xz}}\left\{\frac{1}{2}\rho C_D A_{yz}<\overline{u}_0>|<\overline{u}_0>|+\rho C_M V\frac{d}{dt}<\overline{u}_0>\right\}$

This is the bed shear stress associated with the in-line force (the Morison force) on the lower part of individual roughness elements, the part which remains below the theoretical bed (i.e., Volume 1341, Fig. 10). (Sarpkaya and Isaacson (1981) or Sumer and Fredsøe (1997a) can be consulted for the Morison force). The first part of this force is the drag force and the second part the inertia force. Here C_D is the drag coefficient, and C_M the inertia coefficient which consists of two parts, $C_M=1+C_m$, the first part (i.e., 1) representing the so-called Froude–Krylov force while the second part (C_m, the hydrodynamic or apparent mass coefficient) represents the force to accelerate the water around the roughness element (Sumer and Fredsøe, 1997a). For a free sphere, $C_m=0.5$. Also, in Eq. (7), V is the volume of the individual roughness element below the theoretical bed (i.e., Volume 1341, Fig. 10), A_{xz} is the area of this volume projected on the horizontal plane, and A_{yz} is the area of the same volume projected on the plane perpendicular to the flow direction. The quantity n is the porosity of the bed.

The force coefficients in Eq. (7) were determined from a least-square fit analysis so that the bed friction velocity obtained

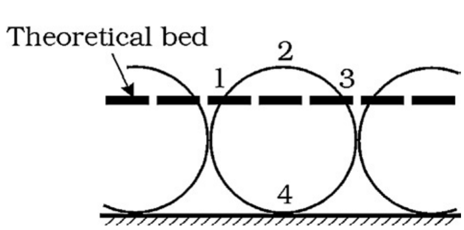

Fig. 10. Definition sketch for the forces on an individual roughness element.

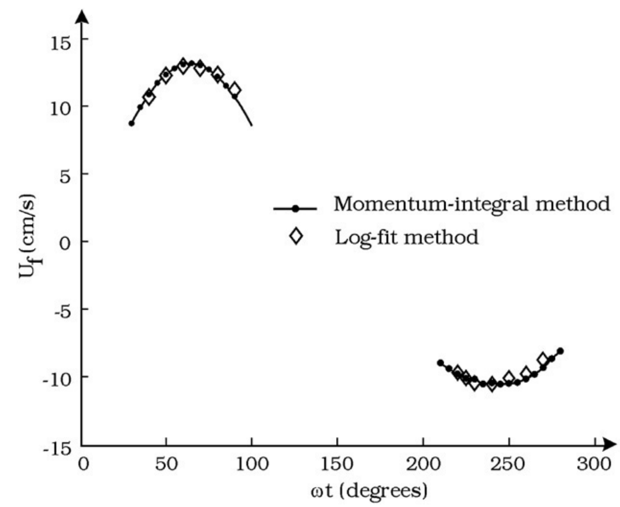

Fig. 11. Comparison of the time variation of the friction velocity found from the log-fit method and that from the momentum-integral method obtained from the least-square fit. Test P1.

from the log-fit method and that from Eq. (7) match. Fig. 11 displays the friction velocity $U_f(\omega t)=\sqrt{\tau_0(\omega t)/\rho}$ from Eq. (7) where $U_f(\omega t)$ data obtained from the log-fit method (diamonds in the figure) are also plotted.

The force coefficients obtained this way are depicted in Table 4.

1. Of particular interest is the fact that the inertia coefficient is, in general, rather small. This may be due to the following two reasons: (1) C_m, the apparent mass coefficient, the second part of the inertia coefficient, is expected to be rather small (definitely smaller than the value for a free sphere/object) because the space between the roughness elements is very limited for the water around the roughness elements to accelerate. (2) The interaction between the wash of the lee-wake water over the roughness elements and the hydrodynamic process generating the hydrodynamic mass may be so that it may result in such small values of C_m. The reduction in C_M is apparently so large that, subtracting the Froude–Krylov part of C_M, namely unity, from the measured values of C_M, the coefficient $C_m=C_M-1$, will take even negative values. This is not surprising, however. For example, in the case of a free circular cylinder, C_m takes

Table 4
Force coefficients

Test	Roughness material	Drag coefficient, C_D	Inertia coefficient, C_M
(1)	(2)	(3)	(4)
S1	Stones	0.4	0.4
S2	”	–	–
S3	”	–	–
P1	Ping-pong balls	0.7	0.1
P2	”	0.7	0.2
P3	”	0.5	0.5
P4	”	0.6	0.1
P5	”	0.5	0.2

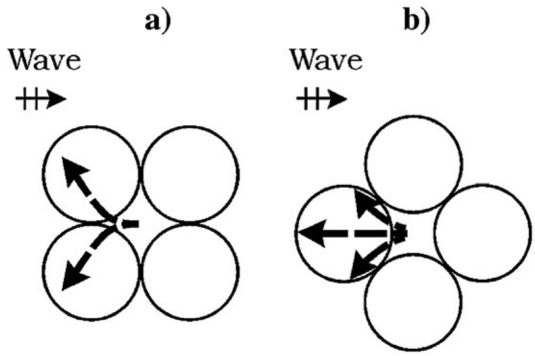

Fig. 12. The way in which the lee-wake water is washed over the spheres during flow reversal. (a): 90°-arrangement. (b): 45°-arrangement.

negative values for the range of the Keulegan–Carpenter number $6 \lesssim KC \lesssim 13$ (Sumer and Fredsøe, 1997a, p. 143) in which

$$KC = \frac{U_m T}{D} \tag{8}$$

in which U_m is the maximum value of the oscillating-flow velocity. It may be noted that KC of the present experiments is $KC = U_m T/D \simeq 27 \times 1.6/3.6 = 12$.

2. The inertia coefficient is distinctly larger for Test P3 (the ping-pong balls, one layer deep, with 45° orientation) than that of the other ping-pong-ball tests. This may be attributed to the fact that the lee-wake water is washed over the roughness elements primarily in the main stream direction (*x*-direction) (Fig. 12b) while, in the other cases, it is washed over the individual roughness elements obliquely (Fig. 12a), an observation made in the present study in a supplementary flow-visualization experiment. In the case of the stones, although smaller than Test P3, the inertia coefficient has a substantial value, and this is also explained as in the case of Test P3.

3. The question how the present force coefficients, C_D and C_M, compare with the existing data will be addressed next. Unfortunately, to the authors' knowledge, no force-coefficient data exists for the present configuration. However, the following two sets of data may be considered for a comparison exercise.

4. The first set of data is from Sarpkaya (1975). He studied forces on *free spheres* in oscillating flows. In Sarpkaya's experiments, the ranges of the Keulegan–Carpenter number and the Reynolds number (the two governing parameters) were as follows: $1 \lesssim KC \lesssim 40$ and $10^3 \lesssim Re \lesssim 5 \times 10^4$ in which $Re = \frac{U_m D}{\nu}$. Sarpkaya gave both C_D and C_M as function of KC. The *Re* number range was in the subcritical regime and therefore the results are uninfluenced by any change in the Reynolds number in this range (Sumer and Fredsøe (1997a) may be consulted for the flow regimes around a body, subcritical, supercritical, etc.). Sarpkaya (1975) noted that no correlation was found between *Re* and the force coefficients, evidently revealing the preceding argument. The second set of data is from the work of Fischer et al. (2002). The latter authors studied forces on a *bottom-mounted single sphere* exposed to an oscillating flow, using direct numerical simulation. They calculated the drag and the lift. The range of KC was from practically 0 to 200 and the calculations were made for $Re = 100$, 200 and 500. These two sets of data are the only ones available for comparison. Sarpkaya's free-sphere force coefficients for the present KC number (KC = 12) read $C_D = 0.6$ and $C_M = 1.2$ while Fischer et al.'s bottom-mounted single sphere drag coefficient for $Re = 500$ (the highest Reynolds number in Fischer et al.'s calculations) reads $C_D = 1.9$ (no inertia coefficient value was reported in Fischer et al.). Although at best suggestive, the present drag coefficient values are not radically different from the preceding drag coefficient values. The apparent difference between the present C_M values and Sarpkaya's $C_M = 1.2$ is, for the most part, due to a completely different flow geometry/environment.

Fig. 13 illustrates the variation of different contributions to the total bed shear stress, (1) the shear stress transferred to the bed by the flow above the theoretical-bed level, (2) the bed shear stress associated with the drag force and (3) that associated with the inertia force on the roughness elements below the theoretical bed (Eq. (7)). This is for Test P3. The picture is much the same for other tests but with a relatively smaller contribution from the inertia.

Regarding the inertia force contribution, we make the following remark. The inertia force contribution is obtained from the least-square exercise where the total force (including the inertia force) is set equal to that obtained from the log-fit method. Since the logarithmic layer is associated with turbulence, then the question is "How can one explain a non-zero (albeit small) inertia contribution, a force which is associated with potential flow?" The inertia force is associated with potential flow only in the case of very small Keulegan–Carpenter numbers, KC. As KC increases, however, the inertia force in the Morison force changes substantially, particularly when KC reaches values to cause vortex shedding, as revealed clearly in Sarpkaya's (1975

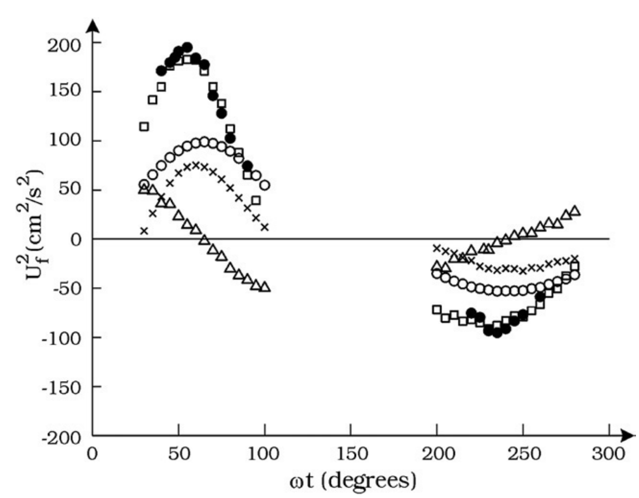

Fig. 13. Contributions of various effects to the total force on individual roughness elements, namely (1) the drag and inertia components of the force on the lower part of individual roughness elements, the part which remains below the theoretical bed (○: contribution from drag force; △: contribution from inertia force), and (2) that transferred from the flow onto the part of the individual roughness elements above the theoretical bed (symbol ×). In addition, ⊡: the friction velocity obtained from the momentum-integral method; and ●: that obtained from the log-fit method. Test P3.

Table 5
The bed friction velocity from different methods

Test	Crest/ trough half periods	Bed friction velocity, U_{fm} (cm/s) from log-fit method	Bed friction velocity, U_{fm} (cm/s) from momentum-integral method	Bed friction velocity, U_{fm} (cm/s) from Reynolds-shear-stress method
(1)	(2)	(3)	(4)	(5)
P1	Crest	13.0	13.2	13.0
	Trough	10.6	10.5	10.3
P2	Crest	13.6	13.9	13.0
	Trough	10.2	10.1	6.8
P3	Crest	14.0	13.5	11.8
	Trough	9.8	9.6	9.8
P4	Crest	13.8	14.3	13.5
	Trough	10.0	9.8	8.3
P5	Crest	13.4	14.2	14.0
	Trough	10.4	9.7	5.9

Ping-pong balls.

and 1986) experiments (see also, e.g., Fig. 4.9 in Sumer and Fredsøe, 1997a,b). This change is related to the lee-wake flow (including the wash of the lee-wake water over the body).

In the asymptotic case where the roughness elements are very small, $a/k_s \to \infty$ (or alternatively $KC \to \infty$), then the bed shear stress is approximated to

$$\tau_0(\omega t) \to \rho \int_0^{\delta} \frac{\partial}{\partial t}[<\overline{u}_0> - <\overline{u}>]\, dy, \tag{9}$$

while, in the other asymptotic case where the roughness elements are very large, so large that $a/k_s \to 0$ (or alternatively $KC \to 0$), then the bed shear stress will be

$$\tau_0(\omega t) \to \frac{1-n}{A_{xz}} \rho C_M V \frac{d}{dt} <\overline{u}_0> \tag{10}$$

(the inertia-dominated regime). In this latter case, the concept of wave boundary layer breaks down, and therefore the bed shear stress will be associated with the ordinary Morison force alone, but obviously only with the inertia component because $KC \to 0$ (the inertia-dominated regime, e.g., Sumer and Fredsøe, 1997a), V here being the volume of the individual roughness element. We shall return to this later in conjunction with the friction factor.

5.3. Bed friction velocity from Reynolds-shear-stress measurements

The friction velocity was also found from the Reynolds shear stress $\left(<-\rho\overline{u'v'}>\right)$ measurements. This was in the ping-pong-ball experiments (Tests P1–P5). No vertical velocity measurements were made in the stone tests, as mentioned previously, and therefore the Reynolds shear stress was not measured. The ensemble- and space-averaged Reynolds shear stress profiles $\left(<-\rho\overline{u'v'}>\right)(y,\omega t)$ were obtained near the bed (see the example given in Fig. 19), and $U_f(\omega t)$ was taken as the maximum value of $\sqrt{<-\rho\overline{u'v'}>(y,\omega t)}$. Subsequently, the maximum value of $U_f(\omega t)$ in phase was taken as U_{fm}.

5.4. Comparison between the three methods

Table 5 compares the bed friction velocities obtained from three different ways.

Clearly, the agreement between the log-fit method and the momentum-integral method is due to the least-square fit of the momentum-integral results to the log-fit results. The agreement between the Reynolds-stress method and the log-fit method is reasonable except Tests P2 and P5 trough-half-period values. No clear explanation has been found for this discrepancy.

Another observation from Table 5 is that the values determined from the Reynolds-stress method are, for the most part, slightly smaller than those from the log-fit method. This is actually not unexpected because the elevation where the Reynolds stress is maximum is not precisely at the bed.

The log-fit results are adopted in the calculation of the wave friction factor, as will be detailed in the next section.

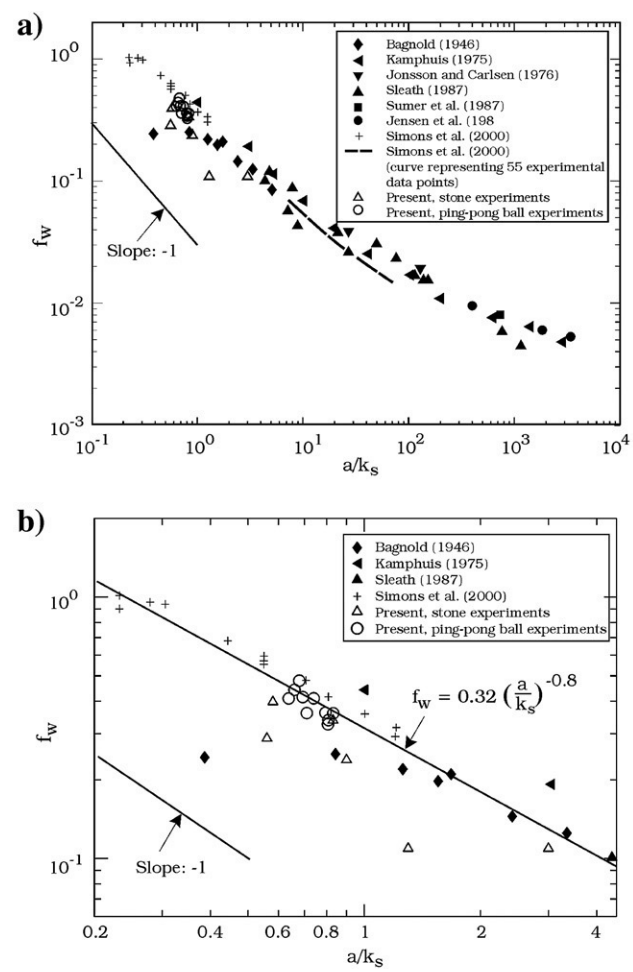

Fig. 14. (a) Friction factor. (b) Friction factor, close-up for small values of a/k_s. The expression $f_w = 0.32(a/k_s)^{-0.8}$ is obtained from a best-fit exercise for the data in the range $0.2 < a/k_s < 10$.

5.5. Wave-friction factor

The wave-friction factor is

$$f_w = 2\left(\frac{U_{fm}}{U_m}\right)^2 \tag{11}$$

(first introduced by Lundgren and Jonsson, 1961).

Tables 2 and 3 (columns 11 in both tables) depict the results regarding the friction factor, calculated based on the friction velocity obtained from the log-fit method (also depicted in Tables 2 and 3, columns 10).

The friction-factor data in Tables 2 and 3 are plotted in Fig. 14a (empty circles and triangles). Fig. 14a also includes the data compiled by Soulsby et al. (1993) and Jensen (1989) plus two more sets of data reported in Simons et al. (2000). Of the data compiled by Soulsby et al. (1993), Simon et al.'s (1988) is not included in Fig. 14a on grounds that it was not pure-wave data. Fig. 14b displays a close-up picture for the range a/k_s from 0.2 to approximately 4.

The following conclusions can be drawn from Fig. 14.

1. The present data are generally consistent with the existing data (see the remarks in the following paragraphs, however).
2. Two points of the present stone data do not agree very well with the trend exhibited by the rest of the data. These data points correspond to the trough half periods of Tests S2 and S3. No clear explanation has been found for this discrepancy. However, we note that the results from the stone experiments need to be interpreted with extra caution on grounds that the space averaging in these tests is not entirely correct, as already pointed out in Section 4. Apart from the previously mentioned two data points of the present study, the present data and Simons et al.'s (2000) data (Fig. 14b) do agree well despite the fact that Simons et al.'s made measurements at smaller scale (roughness elements of 6mm square cross-section, placed at 25mm centres across the line of flow).
3. The results from both the stone and the ping-pong ball experiments seem to be not extremely sensitive to the packing pattern, the packing density, the number of layers and the surface roughness of the roughness elements/stones/spheres; any dependence that may exist seem to be overshadowed by the scatter (albeit small) in the data. The same is also true for the roughness-element shape (Fig. 14a).
4. The present f_w values together with Simons et al.'s (2000) data do not seem to tend to a constant value as $a/k_s \to 0$, contrary to the suggestion made by Kajiura (1968) and Jonsson (1975, 1980), which was based on Bagnold's (1946) data (Fig. 14). We shall return to this point in the following paragraphs.
5. As has been pointed out earlier, the bed shear stress can be written as

$$\tau_0 = \frac{1-n}{A_{xz}}\rho C_M V \frac{d}{dt}\langle\overline{u}_0\rangle \tag{12}$$

as $a/k_s \to 0$ (Eq. (10)). Taking $\langle\overline{u}_0\rangle = U_m \sin(\omega t)$ and $V/A_{xz} = (\pi D^3/6)/(\pi D^2/4) = 2D/3$, the maximum value of the bed shear stress is found to be

$$\tau_{0m} = \frac{2}{3}(1-n)\rho C_M U_m \omega D. \tag{13}$$

Now, although the entire concept of wave boundary layer breaks down for such small values of a/k_s (as was pointed out in Section 5.2), we may, to a first approximation, define a wave-friction factor in the same fashion as in (Eq. (11)), to observe the way in which the friction coefficient varies asymptotically as $a/k_s \to 0$. Taking $D = k_s/2.5$ and recalling $a = U_m/\omega$ the wave-friction factor will be

$$f_w = \frac{2\tau_{0m}}{\rho U_m^2} = \frac{8}{15}(1-n)C_M\left(\frac{a}{k_s}\right)^{-1}. \tag{14}$$

For small values of a/k_s (i.e., for small values of KC), the inertia coefficient, C_M, should go to a constant value (see e.g., Sumer and Fredsøe, 1997a, p. 142). Therefore, for small values of a/k_s, the friction factor should be

$$f_w \propto \left(\frac{a}{k_s}\right)^{-1} \quad \text{as} \quad \frac{a}{k_s} \to 0. \tag{15}$$

Sleath (1984, p. 200) reached the same conclusion from a force balance analysis considering a small segment of bed.

The line with the slope equal to −1 in Fig. 14 illustrates the variation in (Eq. (15)). The present results in Fig. 14 along with Simons et al.'s, Kamphuis' and Bagnold's results (except the two data points to the left (with a/k_s of approximately 0.4 and 0.85) of the Bagnold data) do seem to reveal that f_w tends to go asymptotically to the $\left(\frac{a}{k_s}\right)^{-1}$ variation.

Of the data plotted in Fig. 14, two sets of data for small values of a/k_s, namely Bagnold's data and Kamphuis data (see Fig. 14b), call for special attention.

Bagnold (1946), in his experiments, oscillated an artificially rippled plate (hung vertically in a large tank) by a winding drum and a wire to which weights could be hung, and the mean force per unit area of the plate, τ, was obtained from the measurement of the work done per oscillation in moving the plate through the water (in the calculation of the work done, the effective weight was corrected for mechanical friction). Bagnold plotted τ in the normalized form $k = \tau/(\rho\omega^2 a^2)$ against a/λ_r in which λ_r is the wave length of the ripples, the roughness elements in Bagnold's tests. The normalized force k can be converted to the wave-friction factor ($f_w = 2\tau_{0m}/(\rho U^2)$) by

$$f_w = 3.1k \tag{16}$$

considering that the wall shear stress varies sinusoidally, meaning that the mean force per unit area of the plate per oscillation, τ, namely $\tau = \frac{1}{\pi}\int_{-\phi}^{-\phi+\pi}\tau_0(\omega t)d(\omega t)$ is $\tau = 0.637\,\tau_{0m}$ in which ϕ is the phase lead of the bed shear stress over the surface elevation (see the next section). It may be noted that relationships similar to (Eq. (16)) are used to "translate" Bagnold's k values to f_w by Jonsson (1967) and Kajiura (1968), based on energy-dissipation considerations (see also Jonsson, 1975, 1976, 1980 and Skovgaard et al., 1967).

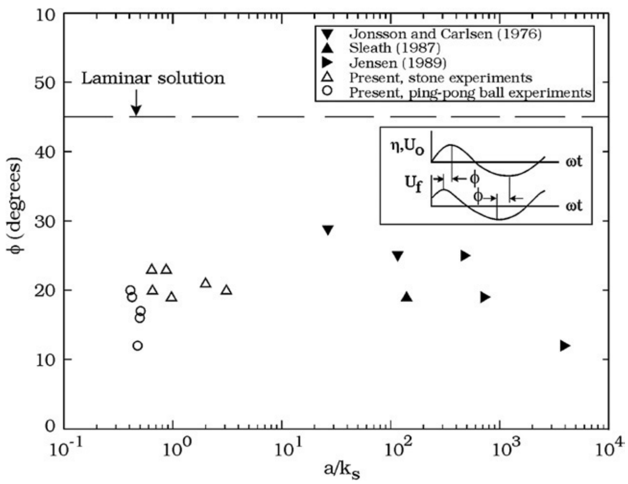

Fig. 15. Phase lead of the friction velocity over the free-surface elevation.

Now, in order to plot Bagnold's data as function of a/k_s, Jonsson (1967) first converted a/λ_r to a/H_r, using the constant ratio of the ripple-length-to-height ratio in Bagnold's tests, namely $\lambda_r/H_r=6.7$, and then converted it to a/k_s, using the relationship $k_s=4H_r$ between the ripple height and Nikuradse's equivalent sand roughness. Bagnold's data plotted in Fig. 14 (which is taken from Soulsby et al., 1993) is essentially based on the previously mentioned two conversions, i.e., f_w values are obtained from Bagnold's original k values using (Eq. (16)), and corresponding a/k_s values are obtained using the relationship $k_s=4H_r$.

1. First of all, the relationship between the ripple height and Nikuradse's equivalent sand roughness, $k_s=4H_r$, grossly "exaggerates" Nikuradse's equivalent sand roughness of Bagnold's ripples. An earlier study of the authors (Fredsøe et al., 1999), although for steady-current case, indicated that $k_s=2.1H_r$ in one test, $2.2H_r$ in another test and $2.4H_r$ in a third test. If these latter values are taken as the Nikuradse equivalent sand roughness, Bagnold's data points in Fig. 14b will shift markedly to the right; for example the data point at $a/k_s=0.4$ will shift to $a/k_s \cong 0.7$ while the data point at $a/k_s=0.85$ will shift to $a/k_s \cong 1.5$, making Bagnold's data points come closer to the data of the others.

2. Since the force is measured as the work done in moving the plate through the water (the energy dissipation), the inertia component of the force on the plate is clearly not included in Bagnold's measurements. Although it may be relatively small (as implied by the present measurements, e.g., Fig. 13), the inertia force for small values of a/k_s may contribute to the total force.

3. The shape of the roughness elements may be important for very small values of a/k_s (or alternatively the KC number) with regard to the forces on individual elements. Bagnold's roughness elements were 2-dimensional ripples while Kamphuis' roughness elements were stones and the present roughness elements are spheres and stones. It may be noted, however, that no information is yet available on the effect of the roughness shape (spherical shape or ripple shape with various ripple-length-to-height ratios) on forces.

The long-debated controversy around the behaviour of Bagnold's wave-friction factor for small values of a/k_s may be explained by the previously mentioned accounts. Of these, the first two accounts can certainly explain the observed smaller values of Bagnold's wave-friction factor for small values of a/k_s. The effect of shape of the roughness elements on the wave-friction factor (Item 3 above) for small values of a/k_s is unknown although the force on ripples with a large value of ripple-length-to-height ratio may be expected to be relatively smaller than that on spheres/stones in the case of sphere/stone-covered beds.

Regarding Kamphuis' (1975) data, Kamphuis' data points for small values of a/k_s ($a/k_s<3$) appear to give values of f_w a factor of 1.5 larger than the trend from the present data and Bagnold's data. In the experiments reported in Kamphuis (1975), a shear plate was used to measure the bed friction, and the experiments were carried out in an oscillating water tunnel. Gravel/stones the size 0.5mm–46mm were used in the experiments. Kamphuis' data apart from those two points for $a/k_s<3$ agree quite well with the existing data. No clear explanation has been found why Kamphuis' measurements predict the friction coefficient a factor 1.5 larger at this end of his experimental range.

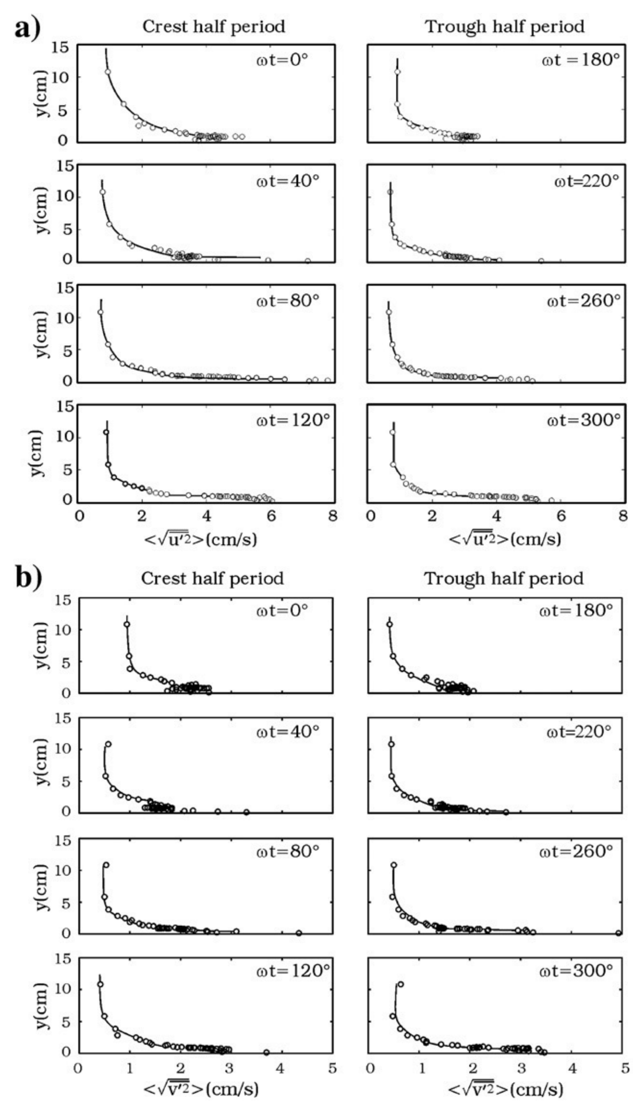

Fig. 16. Turbulence distributions across the depth. Distance y is measured from the theoretical bed. Test P1.

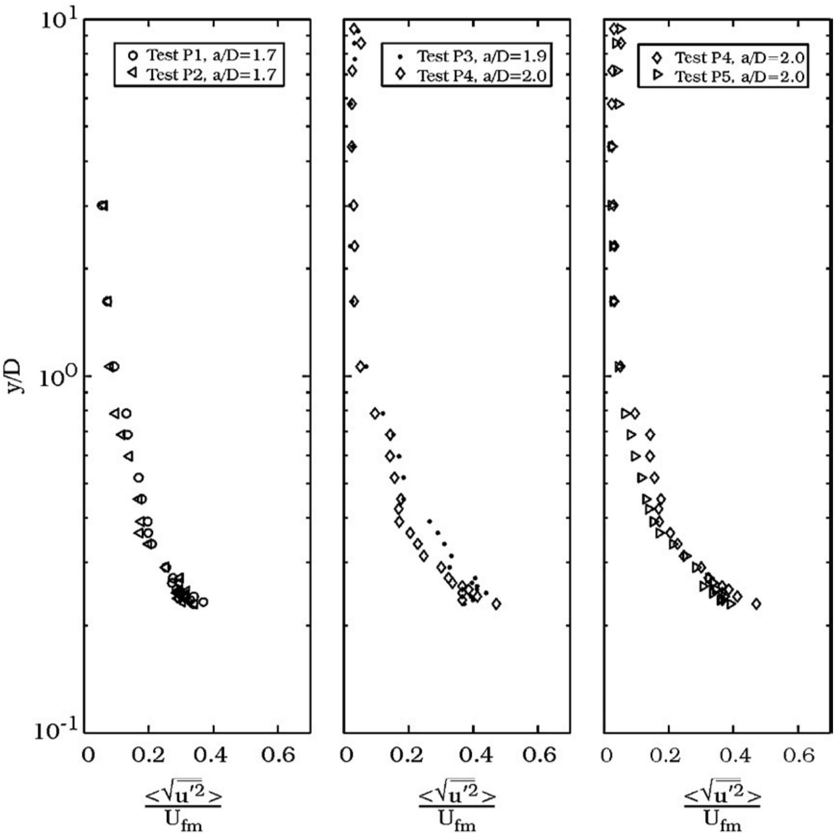

Fig. 17. Turbulence distributions. Comparison. ωt=90°. Distance y is measured from the theoretical bed. Note: the data points below the crest of roughness elements are not shown.

The limiting case $a/k_s \rightarrow 0$ is discussed further in the next section.

Finally, the data plotted in Fig. 14 for small values of a/k_s can be represented by the following empirical expression:

$$f_w = 0.32\left(\frac{a}{k_s}\right)^{-0.8}, \qquad 0.2 < \frac{a}{k_s} < 10 \tag{17}$$

an expression which is slightly different from $f_w = 0.33\left(\frac{a}{k_s}\right)^{-0.84}$ given by Simons et al. (2000). (Eq. (17)) is plotted in Fig. 14b. It may be noted that the friction factor as function of the roughness parameter in the format in (Eq. (17)) was first given by Kamphuis (1975), $f_w = 0.4\left(\frac{a}{k_s}\right)^{-0.75}$ with $\frac{a}{k_s} \leq 100$, on the basis of his data. This expression overpredicts, not surprisingly, the friction factor by a factor of 1.5 for the range indicated in (Eq. (17)).

5.6. Phase difference

There exists a phase difference (ϕ) between the friction velocity, U_f, and the free-surface elevation, η. The friction velocity leads over the free-surface elevation by the angle ϕ (see the definition sketch in Fig. 15), similar to those reported in earlier studies.

The present data are plotted in Fig. 15 together with the results of others (e.g., Jonsson and Carlsen, 1976). Fig. 15 also includes the laminar solution, i.e., ϕ=45° as a reference line. The present results are consistent with the existing data.

Although there is a considerable scatter in the data in Fig. 15, it seems that the phase ϕ does not change radically with a/k_s. This may be due to the fact that the mechanism responsible for the observed phase lead of the friction velocity remains the same, irrespective of the value of the roughness parameter, a/k_s. This mechanism is closely related to the process where the lee-wake water is washed over the roughness elements prior to the flow reversal in the potential-flow region. Since this mechanism

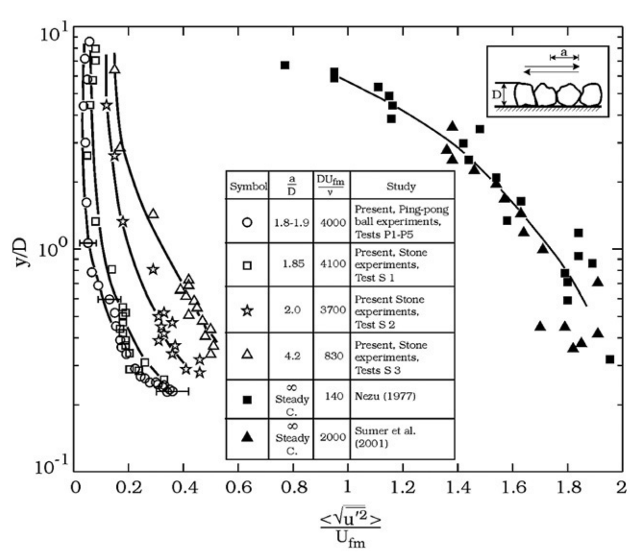

Fig. 18. Turbulence distributions as a function of a/D. The plotted data for each test is the mean of the profiles at ω_t=90° and ω_t=270°. Distance y is measured from the theoretical bed. Note: the data points below the roughness elements are not shown.

does not change with changing the roughness parameter, the phase lead ϕ will therefore remain practically unchanged.

At this juncture, we note the following, regarding the asymptotic case $a/k_s \to 0$. This case can be approached in two ways, either by decreasing a, or by increasing k_s. Consider a small roughness, and gradually decrease a, keeping k_s constant. In this case, the flow regime approaches the laminar-flow regime as $a/k_s \to 0$ (provided that the wall behaves as a hydraulically smooth boundary as $a/k_s \to 0$), and therefore the phase lead should approach the laminar-regime value, $\phi = 45°$, as implied by the closed-triangle symbols in Fig. 15. By contrast, when k_s is increased, keeping a constant, the phase lead remains practically unchanged as $a/k_s \to 0$ (the open symbols in Fig. 15), as interpreted in the preceding paragraph. In the second case the way in which a/k_s goes to 0 is such that the roughness Reynolds number remains larger than 70 so that the wall behaves as a completely rough boundary.

6. Turbulence profiles

6.1. $<\sqrt{\overline{u'^2}}>$ and $<\sqrt{\overline{v'^2}}>$ profiles

Fig. 16 displays the ensemble- and space-averaged turbulence profiles for various values of ωt for the crest and trough half periods in Test P1. Here $u' = u - \overline{u}$ and $v' = v - \overline{v}$, are the fluctuating streamwise and vertical velocity components, respectively; and $\overline{u'^2}$ and $<\sqrt{\overline{u'^2}}>$ (and similarly $\overline{v'^2}$ and $<\sqrt{\overline{v'^2}}>$ are defined in the same fashion as in Eqs. (2), (3), and (4).

Fig. 16 reveals the same picture as in the previous investigations (e.g., Sleath, 1987 and Jensen et al., 1989); that is, turbulence is generated near the bottom and transported into

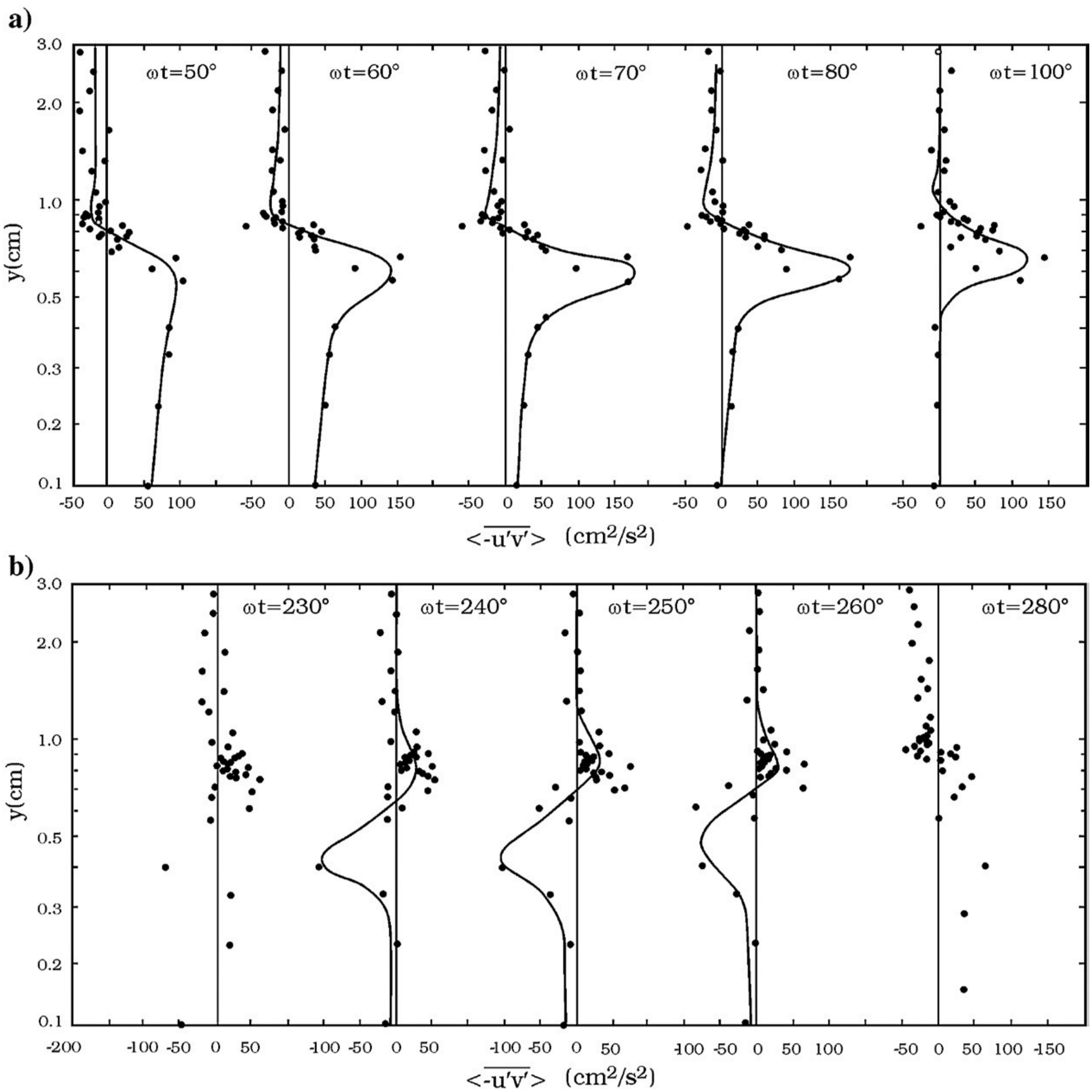

Fig. 19. Reynolds-stress distribution across the depth. Distance y is measured from the theoretical bed. Test P1.

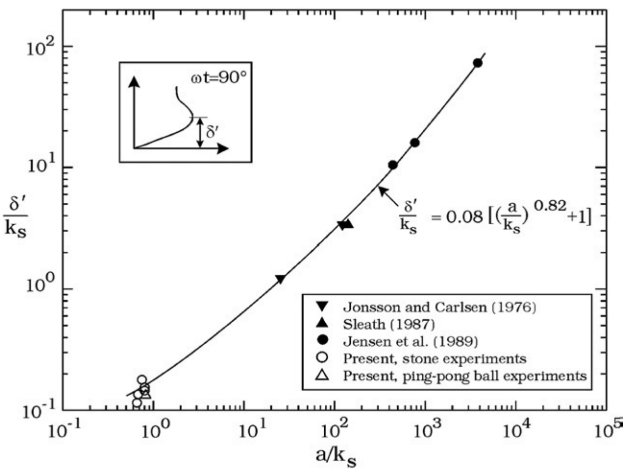

Fig. 20. Boundary-layer thickness.

the main body of the water by diffusion. Some turbulence is retained in the free-stream region at the end of each half cycle, in much the same way as described in e.g. Sleath (1987) and Jensen et al. (1989).

Fig. 17 compares turbulence profiles (the streamwise component) for three different sets of tests: (1) Fig. 17a compares Test P1 (one-layer ping-pong balls) and Test P2 (two layers ping-pong balls); (2) Fig. 17b compares Test P3 (45° orientation) and Test P4 (90° orientation); and (3) Fig. 17c Test P4 (smooth-surface ping-pong balls) and Test P5 (rough-surface ping-pong balls). These figures indicate that the turbulence profiles are practically the same, irrespective of the number of layers, the orientation of the ping-pong balls and the surface roughness of the ping-pong balls. The profiles in Fig. 17 are given for the phase value of $\omega t=90°$. Profiles for other phase values exhibit the same behaviour.

Fig. 18 compares the turbulence profiles for the present tests, to illustrate the dependence of turbulence on the roughness parameter a/k_s (or alternatively a/D) (turbulence is represented in the figure by $<\sqrt{\overline{u'^2}}>/U_{fm}$; recall (Section 2.3) that there are no v' measurements and therefore no v′ and $u'v'$ profiles in the stone experiments). The plotted data in Fig. 18 for each test is the mean of the profiles at $\omega t=90°$ and $\omega t=270°$. The turbulence velocity is normalized by the maximum value of the friction velocity, U_{fm} (the latter is taken as the mean of the crest and trough values, columns 15, Tables 2 and 3). Fig. 18 also includes two sets of data from the steady-current boundary-layer research, namely Nezu (1977) and Sumer et al. (2001), for comparison. The roughness Reynolds numbers of the data plotted in the figure fall in the range $DU_{fm}/\nu>70$, and therefore the bed in all the tests acted as a completely rough boundary.

Fig. 18 shows that the turbulence increases with increasing a/D. This is because the larger the value of the parameter a/D, the larger the Keulegan–Carpenter number, and the larger the number of vortices shed into the main body of the water from the bed (Sumer and Fredsøe, 1997a). Therefore, the turbulence should increase with increasing a/D. In the asymptotic case when $a/D\to\infty$, the quantity $<\sqrt{\overline{u'^2}}>/U_{fm}$ is expected to approach the profile measured in the case of the steady current. Fig. 18 apparently reveals this.

6.2. $<-\overline{u'v'}>$ *profiles*

Fig. 19 displays the time development of the vertical distribution of Reynolds shear stress $<-\overline{u'v'}>$ near the bed for phase values covering $\omega t=50°–100°$ for the crest half period and $\omega_t=230°–280°$ for the trough half period. Although there is considerable scatter (due to the relatively small sample size), the trend is clear. The maximum value of $<-\overline{u'v'}>$ occurs around $y\simeq 0.6$cm (for the crest half period) and $y\simeq 0.5$cm (for the trough half period) (or alternatively, at 0.2cm (for the crest half period) and 0.3cm (for the trough half period) below the top of the roughness elements), y being the vertical distance measured from the theoretical bed. It may be noted that the shear stress picture in Fig. 19 is consistent with the velocity picture given in Figs. 5 and 6.

7. Boundary-layer thickness

Fig. 20 shows the data regarding the boundary-layer thickness. The boundary-layer thickness is defined as the distance from the theoretical bed to the point where $<u>$ is maximum at the phase value $\omega t=90°$, similar to our previous work (e.g. Sumer et al., 1987 and Jensen et al., 1989) (see the definition sketch in Fig. 20). Symbol δ' is used to avoid confusion with the boundary-layer thickness δ used in conjunction with the momentum-integral method (Fig. 9). Fig. 20 includes also other data. The present data appears to be in accord with the existing data, revealing the smaller the value of the parameter a/k_s, the smaller the boundary-layer thickness. The present data suggest that δ' in the case of stone-covered seabed where the roughness parameter can be as small as a/k_s ($a/k_s=O(1)$, or smaller) is $\delta'=O(0.5D)$ or smaller.

Finally, the data in Fig. 20 can be represented by the following empirical expression

$$\frac{\delta'}{k_s}=0.08\left[\left(\frac{a}{k_s}\right)^{0.82}+1\right],\qquad 0.5<\frac{a}{k_s}<5000. \tag{18}$$

This equation is actually a slightly different version of the expression given in the book of Fredsøe and Deigaard (1992) to cover the new set of data corresponding to small values of a/k_s.

8. Steady streaming

The steady streaming is defined by

$$U_s(y)=\frac{1}{T}\int_0^T <\overline{u}>(y,\omega t)dt. \tag{19}$$

Although the wave-induced flow is cyclic with zero mean velocity, the interaction between the potential flow and the boundary layer leads to a steady flow in the direction of wave propagation with a non-zero mean, the so-called steady streaming in the boundary layer (Longuet-Higgins, 1957). Fig. 21 displays

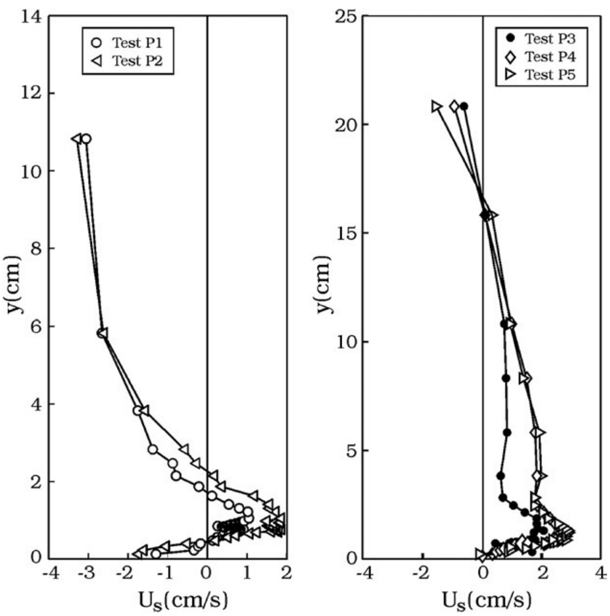

Fig. 21. The steady-streaming velocity profiles. Distance y is measured from the theoretical bed.

the steady-streaming velocity near the bed. The steady-streaming data plotted in the figure come from the ping-pong-ball experiments. The steady streaming was not in the program of the first experimental campaign with the stones, and unfortunately the raw velocity data was not saved for the phase values other than those where the mean and turbulence properties were calculated, and therefore the steady streaming for the stone experiments could not be calculated.

The following conclusions can be drawn from Fig. 21.

1. There exists a steady streaming near the bed in the direction of wave propagation, in agreement with the existing knowledge (Longuet-Higgins, 1957; see also, e.g. Fredsøe and Deigaard, 1992, p. 47).

2. Away from the bed, there is a constant flow in the direction opposite to the wave propagation. This is due to the return flow in the flume. In a confined environment (as in the present wave flumes), a return flow takes place to balance the wave drift, as measured in the previous research (e.g., Sumer and Fredsøe, 1997b; Fredsøe et al., 1999).

3. There are two distinct patterns of the variation of the steady streaming exhibited in Fig. 21: One with a substantial extent of the vertical distance with positive velocities, $U_s>0$ (Tests P3, P4 and P5), and the other with a relatively smaller extent of the vertical distance with $U_s>0$ (Tests P1 and P2). These two groups of experiments essentially differ from each other in two aspects (Table 1):

- Tests P1 and P2 were conducted without the active wave dissipation system (AWACS) while Tests P3, P4 and P5 were conducted with AWACS; and
- Tests P1 and P2 were conducted in Flume B where the onshore end of the flume had a 3.8m long section with a slope of 1:22 (see Fig. 1b) while, in the case of Tests P3, P4 and P5, no such section was present, and the bed was completely horizontal (see Fig. 1c).

To observe the influence of the AWACS on the steady streaming, supplementary tests were carried out in Flume A with and without the AWACS system, and these experiments showed that the steady streaming was practically uninfluenced. Therefore, the distinct difference observed in the behaviour of the steady streaming in the two groups of experiments cannot be explained in terms of the AWACS system.

The difference observed in Fig. 21 can be explained, however, in terms of the sloping bed at the onshore end of the flume in Tests P1 and P2. The return flow in these tests is apparently "enhanced" over this bed section due to gravity because of the sloping bed (a section with a substantial bed slope). When superimposed on the streaming velocity field, this enhanced return flow will induce a constant flow in the direction opposite to the wave propagation very near the bed, resulting in the streaming velocity profile observed for Tests P1 and P2 in Fig. 21.

4. The steady streaming near the bed is markedly smaller in the case of the 45°-arrangement (Test P3). This may be explained by the more strong reverse flow of the lee-wake water prior to the flow reversal in the 45°-arrangement.

5. The steady streaming is relatively smaller in the case of the one-layer ping-pong-ball roughness (Test P1) than in the case of the two-layer ping-pong-ball roughness (Test P2). No clear explanation has been found for this.

6. The theoretical value for the steady-streaming velocity can be found from the relationship given by Brøker Hedegaard (1985) (Fredsøe and Deigaard (1992, p.48) for a turbulent boundary layer. Brøker's diagram does not cover small values of a/k_s. In the calculations the results are found from an extrapolation of Brøker's curve to the present values of a/k_s. The results vary between $U_s=1.7$ and 1.9cm/s. Since the theoretical streaming velocity does not take into account of the return flow, the return flow, O(2cm/s), from Fig. 21 needs to be added to the measured near-bed steady streaming. With this, the measured steady streaming near the bed in Fig. 21 (the actual measured steady-streaming velocity) is found to be $U_s=3$cm/s for Test P1; 3.8cm/s for Test P2; 4.0cm/s for Test P3; 4.6cm/s for Test P4; and 4.9cm/s for Test P5. Comparing the latter values (O(4cm/s)) with the theoretical value (O(2cm/s)), it is seen that the measured values are a factor 2 larger than the theoretical value calculated from Brøker's relation. The discrepancy between the measured value and the calculated value may be attributed to the extrapolation of Brøker's curve to the present small values of the roughness.

9. Application to stone stability

The present result regarding the wave friction factor (Eq. (17)) may be used to predict the stone stability for bed/protection stones under waves. This can be done using the Shields criterion for the initiation of motion; namely stones will be stable when

$$\theta < \theta_{cr} \tag{20}$$

in which θ is the Shields parameter defined by

$$\theta = \frac{U_{\mathrm{fm}}^2}{g(s-1)D} \tag{21}$$

in which s is the specific gravity of stones and g is the acceleration due to gravity. θ_{cr} is the critical value of the Shields parameter corresponding to the initiation of motion at the bed, and the friction velocity, U_{fm}, is

$$U_{\mathrm{fm}} = \sqrt{\frac{f_{\mathrm{w}}}{2}}U_{\mathrm{m}} \tag{22}$$

where the friction factor is given by (Eq. (17)) provided that $0.2 < a/k_{\mathrm{s}} < 10$.

Considering that the stone Reynolds number, DU_{fm}/ν, is typically very large for stone protection (definitely larger than $DU_{\mathrm{fm}}/\nu > 70$, a completely rough boundary), the critical value of the Shields parameter can be taken as $\theta_{\mathrm{cr}}=0.045$ (see, e.g., Fig. 1.2 in Sumer and Fredsøe, 2002). Therefore, stones will be stable when

$$\theta < 0.045. \tag{23}$$

In practice the so-called mobility number (Nielsen, 1992) also is used in describing sediment motion including the initiation of motion:

$$\psi = \frac{U_{\mathrm{m}}^2}{g(s-1)D} \tag{24}$$

in which U_{m} is the maximum value of the orbital velocity of water particles at the bed (i.e., the velocity just outside the boundary layer). The critical value of the mobility number corresponding to the initiation of motion at the bed is ψ_{cr}, and therefore stones will be stable when

$$\psi < \psi_{\mathrm{cr}}. \tag{25}$$

The critical value of the mobility number may be found from the critical value of the Shields parameter:

$$\psi_{\mathrm{cr}} = \frac{U_{\mathrm{m,cr}}^2}{g(s-1)D} = \frac{\frac{2}{f_{\mathrm{w}}}U_{\mathrm{fm,cr}}^2}{g(s-1)D} = \frac{2}{f_{\mathrm{w}}}\frac{U_{\mathrm{fm,cr}}^2}{g(s-1)D} = \frac{2}{f_{\mathrm{w}}}\theta_{\mathrm{cr}} \tag{26}$$

in which $\theta_{\mathrm{cr}}=0.045$ (Eq. (23)) and $f_{\mathrm{w}} = 0.32\left(\frac{a}{k_{\mathrm{s}}}\right)^{-0.8}$ (Eq. (17)). Taking $k_{\mathrm{s}}=2.5D$, then the critical value of the mobility number will be

$$\psi_{\mathrm{cr}} = 0.135\left(\frac{a}{D}\right)^{0.8}, \quad O(0.5) < \frac{a}{D} < O(25). \tag{27}$$

The latter equation (and therefore the stability criterion (Eq. (25)) may prove more "handy" to use in practice as it requires only U_{m} and a, the orbital-velocity amplitude and the orbital-displacement amplitude at the bed, respectively. Caution must be exercised with the range of a/D where (Eq. (27)) is valid. For values of a/D even smaller than $O(0.5)$, it is expected that the power 0.8 in (Eq. (27)) should go to 1, as f_{w} in this case tends to go asymptotically to $\left(\frac{a}{k_{\mathrm{s}}}\right)^{-1}$, as discussed earlier. Regarding the upper bound of the range, it is anticipated that this value corresponds to fairly small stone sizes and therefore a/D can hardly take values larger than $O(25)$. Nevertheless, if a/D takes values larger than $O(25)$, f_{w} can be calculated, using one of the empirical formulae given in the literature, such as $f_{\mathrm{w}} = 0.237\left(\frac{a}{k_{\mathrm{s}}}\right)^{-0.52}$ (Soulsby, 1997).

Numerical example. The following numerical example illustrates the calculation of D for typical storm values of the input quantities. Consider $U_{\mathrm{m}}=2.5$m/s, and $T=8.5$s (a set of storm-wave conditions probably near breaking). The amplitude of the orbital motion of water particles can, to a first approximation, be calculated from $a=U_{\mathrm{m}}T/(2\pi)=2.5\times 8.5/(2\pi)=3.4$m. The critical condition is attained when the mobility number is equal to the critical value (from Eqs. (24) and (27)):

$$\frac{U_{\mathrm{m}}^2}{g(s-1)D} = 0.135\left(\frac{a}{D}\right)^{0.8}. \tag{28}$$

Inserting $U_{\mathrm{m}}=2.5$m/s, $a=3.4$m, $g=9.81$m/s^2 and $s=2.65$, the solution of the preceding equation gives $D=1.5$m, meaning that the stones larger than 1.5m will be stable (check for the value of a/D: the ratio $a/D=3.4/1.5=2.3$, and therefore in the range where (Eq. (27)) is valid.)

10. Conclusions

1. Ensemble- and space-averaged velocity profiles measured in the experiments indicate that the conventional logarithmic law is satisfied near the bed from phase values ωt larger than 40° for the present roughness values as small as $a/k_{\mathrm{s}}=O(0.5)$.
2. The classic log-fit exercise indicates that Nikuradse's equivalent roughness value is $k_{\mathrm{s}}=2.5D$ for the ping-pong balls and $k_{\mathrm{s}}=(2.0\text{–}2.3)D$ for the stones used in the tests.
3. The preceding exercise also shows that the theoretical bed is located at $0.25D$ below the crests of the stones. The latter figure is $0.23D$ for the ping-pong balls.
4. The friction velocity determined from the log-fit method and that obtained from the Reynolds-stress measurements generally agree reasonably well although the latter is slightly smaller than the former. This is due to the fact that the location where the Reynolds stress is maximum is not precisely at the bed.
5. The friction velocity is also obtained from the momentum-integral method. This involves (1) the contribution from the shear stress transferred from the flow to the bed at the theoretical-bed level, and (2) that due to the in-line (the Morison) force on the lower part of individual roughness elements, the part which remains below the theoretical-bed level.
6. In conjunction with the previously mentioned in-line force, a least-square-fit analysis indicated that the in-line force coefficients are $C_{\mathrm{D}}=O(0.5)$ and $C_{\mathrm{M}}=O(0.1)$ with the exception that $C_{\mathrm{M}}=0.5$ for the 45°-arrangement of ping-pong balls and $C_{\mathrm{M}}=0.4$ for the stones. Even with these values, the inertia component of the in-line force is a small fraction of the actual/total force on the bed (Fig. 13) for the tested values of the bed roughness in the present study.
7. The friction factor for small values of the parameter a/k_{s} does not seem to tend to a constant value as $a/k_{\mathrm{s}}\to 0$ (contrary to the suggestion made by some previous investigators). The

present friction-factor data seems to indicate that the friction factor varies with a/k_s like $\left(\frac{a}{k_s}\right)^{-1}$ as $\frac{a}{k_s}\to 0$.

8. The friction factor is not extremely sensitive to the packing pattern, the packing density, the number of layers and the surface roughness of the roughness elements/stones/spheres; any dependence that may exist seem to be overshadowed by the scatter (albeit small) in the data.

9. The phase lead of the bed friction velocity over the surface elevation, ϕ, does not seem to change radically with a/k_s. The quantity ϕ is found to be in the range 12°–23° for the tested values of $a/k_s=0.6$–3, and is not extremely sensitive to the packing pattern, the packing density, the number of layers and the surface roughness of the roughness elements/stones/spheres.

10. Turbulence increases with increasing values of a/k_s (or alternatively with increasing values of a/D), and tends to that measured in the case of steady currents, as $a/k_s\to\infty$.

11. Turbulence profiles obtained in the present study indicate that they are practically the same, irrespective of the number of layers, the orientation of the ping-pong balls and the surface roughness of the ping-pong balls.

12. The present data suggest that the wave-boundary-layer thickness, δ', in the case of stone-covered seabed where the roughness parameter can be as small as $a/k_s=O(1)$ (or smaller) is $\delta'=O(0.5D)$ (or smaller).

13. There exists a steady streaming near the bed in the direction of wave propagation, in agreement with the existing work.

14. The steady streaming is markedly smaller in the case of the 45°-arrangement of the ping-pong ball roughness than in the other cases.

15. The steady streaming is relatively smaller in the case of the one-layer ping-pong-ball roughness than in the case of the two-layer situation.

Acknowledgments

This study was partially funded by the Research Frame Program "Exploitation and Protection of Coastal Zones" (EPCOAST) of the Danish Research Council for Technology and Production Sciences (FTP) (formerly Danish Research Council, STVF). Ms. Figen Hatipoglu's stay at the Technical University of Denmark has been supported first by two postdoctoral scholarships from Turkey (one from the Scientific and Technical Research Council of Turkey (TUBITAK) and the other from the Istanbul Technical University Research Fund), and later by EPCOAST.

References

Bagnold, R.A., 1946. Motion of waves in shallow water. Interaction between waves and sand bottoms. Proc. Roy. Soc. Ser. A 187, 1–15.

Bayazit, M., 1976. Free surface flow in a channel of large relative roughness. J. Hydraul. Res. 14 (2), 115–125.

Bayazit, M., 1983. Flow structure and sediment transport mechanics in steep channels. Mechanics of Sediment Transport, Proc. of Euromech 156, Istanbul, 12–14. July 1982. A.A. Balkema, Rotterdam, pp. 197–206.

Brøker Hedegaard, I., 1985. Wave generated ripples and resulting sediment transport in waves. Series paper, vol. 36. Institute of Hydrodynamics and Hydraulic Engineering, Technical University of Denmark, Lyngby.

Fischer, P.F., Leaf, G.K., Restrepo, J.M., 2002. Forces on particles in oscillatory boundary layers. J. Fluid Mech. 468, 327–347.

Fredsøe, J., 1984. Turbulent boundary layer in wave-current motion. J. Hydraul. Eng. ASCE 110 (8), 1103–1120.

Fredsøe, J., Deigaard, R., 1992. Mechanics of Coastal Sediment Transport. World Scientific.

Fredsøe, J., Andersen, K.H., Sumer, B.M., 1999. Wave plus current over ripple-covered bed. Coast. Eng. 38, 177–221.

Grass, A.J., 1971. Structural features of turbulent flow over smooth and rough boundaries. J. Fluid Mech. 50, 233–255.

Hatipoglu, F., Sumer, B.M., Fredsøe, J., 2004. Wave boundary layers over a bed with large roughness. 29th International Conference on Coastal Engineering (ICCE 2004), Abstracts, 19–24.September, 2004, Lisbon, Portugal. Paper, vol. 202.

Jensen, B.L., 1989. Experimental Investigation of Turbulent Oscillatory Boundary Layers. Technical University of Denmark, Institute of Hydrodynamics and Hydraulic Engineering, Lygnby, Denmark. Series Paper, vol. 45.

Jensen, B.L., Sumer, B.M., Fredsøe, J., 1989. Turbulent oscillatory boundary layers at high Reynolds numbers. J. Fluid Mech. 206, 265–297.

Justesen, P., 1988a. Turbulent Wave Boundary Layers. Technical University of Denmark, Institute of Hydrodynamics and Hydraulic Engineering, Lygnby, Denmark. Series Paper, vol. 43.

Justesen, P., 1988b. Prediction of turbulent oscillatory flow over rough beds. Coast. Eng. 12 (3), 257–284.

Jonsson, I.G., 1967. Wave Boundary Layers and Friction Factors. Proc. 10th Conf. on Coastal Engineering, Tokyo, vol. I, pp. 127–148.

Jonsson, I.G., 1975. The wave friction factor revisited. Technical University of Denmark, Institute of Hydrodynamics and Hydraulic Engineering, Lygnby, Denmark. Progress Report, vol. 37, pp. 3–8.

Jonsson, I.G., 1976. Discussion of "Friction factor under oscillatory waves" by J.W. Kamphuis. J. Waterw., Port, Coast., Ocean Div. ASCE 102 (WW1), 108–109.

Jonsson, I.G., 1980. A new approach to oscillatory rough turbulent boundary layers. Ocean Eng. 7, 109–152.

Jonsson, I.G., Carlsen, N.A., 1976. Experimental and theoretical investigations in an oscillatory turbulent boundary layer. J. Hydraul. Res. 14, 45–60.

Kajiura, K., 1968. A model of bottom boundary layer in water waves. Bull. Earthq. Res. Inst. 46, 75–123.

Kamphuis, J.W., 1975. Friction factor under oscillatory waves. J. Waterw., Port, Coast., Ocean Div. ASCE 101 (WW2), 135–144.

Lambe, T.W., Whitman, R.V., 1969. Soil Mechanics. John Wiley and Sons, Inc.

Longuet-Higgins, M.S., 1957. The mechanics of the boundary layer near the bottom in a progressive wave. Proc. 6th International Conference on Coastal Engineering, Gainesville, Palm Beach and Miami Beach, Florida, December 1957, pp. 184–193.

Lundgren, H., Jonsson, I.G., 1961. Bed shear stress induced by a wave motion. Coastal Engineering Laboratory, Technical University of Denmark. Basic Research-Progress Report, vol. 1, pp. 3–5.

Monin, A.S., Yaglom, A.M., 1973. Statistical Fluid Mechanics: Mechanics of Turbulence. MIT Press, Cambridge, Mass.

Nezu, I. (1977). Turbulence Structures in Open Channel Flows. PhD. Thesis, Kyoto University, Kyoto, Japan.

Nielsen, P., 1992. Coastal Bottom Boundary Layers and Sediment Transport. World Scientific.

Sarpkaya, T., 1975. Forces on cylinders and spheres in a sinusoidally oscillating fluid. Transactions of the ASME, Journal of Applied Mechanics, March 1975, pp. 32–37.

Sarpkaya, T., 1986. Force on a circular cylinder in viscous oscillatory flow at low Keulegan–Carpenter numbers. J. Fluid Mech. 165, 61–71.

Sarpkaya, T., Isaacson, M., 1981. Mechanics of Wave Forces on Offshore Structures. Van Nostrand Reinhold Company.

Schaffer, H.A., Stolborg, T., Hyllested, P., 1994. Simultaneous generation and active absorption of waves in flumes. Proc. International Symposium: Waves-Physical and Numerical Modelling. University of British Columbia, Vancouver, Canada, pp. 90–99.

Simons, R.R., Kyriacou, A., Soulsby, R.L., Davies, A.G., 1988. Predicting the nearbed turbulent flow in waves and currents. Proc. I.A.H.R. Symposium on Mathematical Modelling of Sediment Transport in the Coastal Zone, Copenhagen, pp. 33–47.

Simons, R., Myrhaug, D., Thais, L., Chapalain, G., Holmedal, L.-E., MacIver, R., 2000. Bed friction in combined wave-current flows. Coastal Engineering Conference, ASCE, July 16–21, 2000, Sydney, Australia. Proceedings, vol. 1, pp. 216–226.
Skovgaard, O., Jonsson, I.G., Bertelsen, J.A., 1967. Closure to “Computation of wave heights due to refraction and friction”. J. Waterw., Port, Coast., Ocean Div. ASCE 102 (WW1), 108–109.
Sleath, J.F.A., 1984. Sea Bed Mechanics. John Wiley & Sons.
Sleath, J.F.A., 1987. Turbulent oscillatory flow over rough beds. J. Fluid Mech. 182, 360–409.
Soulsby, R.L., 1997. Dynamics of Marine Sands. Thomas Telford, London.
Soulsby, R.L., Hamm, L., Klopman, G., Myrhaug, D., Simons, R.R., Thomas, G.P., 1993. Wave-current interaction within and out-side the bottom boundary layer. Coast. Eng. 21, 41–69.
Sumer, B.M., Fredsøe, J., 1997a. Hydrodynamics Around Cylindrical Structures. World Scientific.
Sumer, B.M., Fredsøe, J., 1997b. Scour Around a Large Vertical Circular Cylinder in Waves. 16th International Conference on Offshore Mechanics and Arctic Engineering, Yokohama, Japan, April 13–18, vol. I-A, pp. 57–64.
Sumer, B.M., Fredsøe, J., 2002. The Mechanics of Scour in the Marine Environment. World Scientific.
Sumer, B.M., Jensen, B.L., Fredsøe, J., 1987. Turbulence in oscillatory boundary layers. In: Comte-Bellot, C., Mathieu, J. (Eds.), Advances in Turbulence. Springer-Verlag, Berlin, pp. 556–567.
Sumer, B.M., Cokgor, S., Fredsøe, J., 2001. Suction removal of sediment from between armour blocks. J. Hydraul. Eng. ASCE, 127 (4), 293–306.

Glossary

a: Amplitude of the orbital motion of water particles at the bed. Measured at $y=4$ cm from the bed in the present tests.
A_{xz}: Projected area in plan view of the individual roughness element.
A_{yz}: Area of the same volume projected on the plane perpendicular to the flow direction.
C_D: Drag coefficient.
C_M: Inertia coefficient.
D: Mean size of the roughness element, actual roughness height.
f_w: Wave friction factor.
H: Wave height.
KC: Keulegan–Carpenter number.
k_s: Nikuradse’s equivalent sand roughness.
N: Number of cycles sampled.
Re: Reynolds number.
t: Time.
u: Horizontal velocity.
u': Fluctuating horizontal velocity.
$\overline{u}$: Ensemble-averaged horizontal velocity.
v: Vertical velocity.
v': Fluctuating vertical velocity.
$<\overline{u}>$: Space- and ensemble-averaged streamwise velocity.
$<\overline{u}_0>$: Potential-flow velocity just outside the boundary layer.
U: Orbital velocity of water particles at the bed.
U_f: Friction velocity.
U_{fm}: Maximum value of the friction velocity.
U_m: Maximum value of the orbital velocity at the bed. Measured at $y=4$ cm from the bed in the present tests.
U_s: Streaming velocity.
V: Volume of the individual roughness element below the theoretical bed, or, the volume of the individual roughness element as $a/k_s \rightarrow 0$.
y: Vertical distance measured from the theoretical bed.
y': Vertical distance measured from the base bottom.
y_1: Distance between the theoretical bed and the base bottom.
δ: Boundary-layer thickness (Fig. 9).
δ': Boundary-layer thickness (Fig. 20).
η: Surface elevation.
κ: Kármán constant.
ν: Kinematic viscosity.
ρ: Fluid density.
τ_0: Bed shear stress.
τ_{0m}: Maximum value of the bed shear stress.
ϕ: Phase lead of the friction velocity over the surface elevation.
ω: Angular frequency.
Δy: Distance of the theoretical bed from the top of the stones.